ΕΘΝΙΚΟ ΜΕΤΣΟΒΙΟ ΠΟΛΥΤΕΧΝΕΙΟ

ΣΧΟΛΗ ΕΦΑΡΜΟΣΜΕΝΩΝ ΜΑΘΗΜΑΤΙΚΩΝ ΚΑΙ ΦΥΣΙΚΩΝ ΕΠΙΣΤΗΜΩΝ

ΣΧΟΛΗ ΜΗΧΑΝΟΛΟΓΩΝ ΜΗΧΑΝΙΚΩΝ

ΕΚΕΦΕ «ΔΗΜΟΚΡΙΤΟΣ»

ΙΝΣΤΙΤΟΥΤΟ ΝΑΝΟΕΠΙΣΤΗΜΗΣ ΚΑΙ ΝΑΝΟΤΕΧΝΟΛΟΓΙΑΣ

ΙΝΣΤΙΤΟΥΤΟ ΠΥΡΗΝΙΚΗΣ ΚΑΙ ΣΩΜΑΤΙΔΙΑΚΗΣ ΦΥΣΙΚΗΣ

Διατμηματικό Πρόγραμμα Μεταπτυχιακών Σπουδών

«Φυσική και Τεχνολογικές Εφαρμογές»

Η επιλογή νέας φυσικής στο πείραμα ATLAS του LHC με τον αναβαθμισμένο ανιχνευτή μιονίων New Small Wheel

Μεταπτυχιακή διπλωματική εργασία

της **Φωτεινής-Φαίδρας Τράντου**

Επιβλέπων :

Θεόδωρος Γέραλης

Ερευνητής Α', ΙΠΣΦ, ΕΚΕΦΕ Δημόκριτος

Αθήνα, Φεβρουάριος, 2022

ΕΘΝΙΚΟ ΜΕΤΣΟΒΙΟ ΠΟΛΥΤΕΧΝΕΙΟ

ΣΧΟΛΗ ΕΦΑΡΜΟΣΜΕΝΩΝ ΜΑΘΗΜΑΤΙΚΩΝ ΚΑΙ ΦΥΣΙΚΩΝ ΕΠΙΣΤΗΜΩΝ

ΣΧΟΛΗ ΜΗΧΑΝΟΛΟΓΩΝ ΜΗΧΑΝΙΚΩΝ

ΕΚΕΦΕ «ΔΗΜΟΚΡΙΤΟΣ»

ΙΝΣΤΙΤΟΥΤΟ ΝΑΝΟΕΠΙΣΤΗΜΗΣ ΚΑΙ ΝΑΝΟΤΕΧΝΟΛΟΓΙΑΣ

ΙΝΣΤΙΤΟΥΤΟ ΠΥΡΗΝΙΚΗΣ ΚΑΙ ΣΩΜΑΤΙΔΙΑΚΗΣ ΦΥΣΙΚΗΣ

Διατμηματικό Πρόγραμμα Μεταπτυχιακών Σπουδών

«Φυσική και Τεχνολογικές Εφαρμογές»

Η επιλογή νέας φυσικής στο πείραμα ATLAS του LHC με τον αναβαθμισμένο ανιχνευτή μιονίων New Small Wheel

Μεταπτυχιακή διπλωματική εργασία

της **Φωτεινής-Φαίδρας Τράντου**

Εγκρίθηκε από την τριμελή εξεταστική επιτροπή στις 25 Φεβρουαρίου 2022.

……..…………….	…………………..	……….………….
Θεόδωρος Γέραλης	Γεώργιος Σταυρόπουλος	Θεόδωρος Αλεξόπουλος

Αθήνα, Φεβρουάριος, 2022

Acknowledgments

Concluding this master thesis, I would like to express my gratitude to all those who helped me and supported me during its preparation.

I would first like to thank my supervisor Theodoros Geralis, Director of Research at the Institute of Nuclear and Particle Physics (INPP) - NCSR “Demokritos”, for entrusting me with this thesis subject and for giving me the opportunity to conduct my research at the European Organization for Nuclear Research - CERN. I am sincerely grateful for his guidance, his advices and the constant assistance that he provided throughout my thesis preparation.

I would also like to thank Georgios Stavropoulos, Director of Research at the INPP- NCSR “Demokritos”, and Theodoros Alexopoulos, professor at the National Technical University of Athens, for assisting in the evaluation of this master thesis and providing crucial commentary for its completion.

My gratitude extends to the NCSR ATLAS Demokritos group members for the constructive discussions and feedback they provided to my postgraduate work. I would particularly like to thank Olga Zormpa for her patience and invaluable help.

Finally, I would like to thank my family and friends for their unwavering support and belief in me. This accomplishment would not have been possible without their love and encouragement.

Abstract

This master thesis was prepared within the framework of the interdepartmental postgraduate program: "Physics and Technological Applications" of the National Technical University of Athens in collaboration with the National Center for Research in Natural Sciences "Demokritos". It was carried out entirely at CERN in the year 2020-2021.

The ATLAS detector, part of the Large Hadron Collider (LHC) at CERN, will undergo a series of upgrades in order to maintain high physics performance at High Luminosity - LHC (HL-LHC) conditions. The goal of the HL-LHC project is to improve particle detection and the ability to observe rare events by increasing the number of proton-proton collisions at the LHC.

The aim of this thesis is to study the trigger system of the upgraded muon spectrometer New Small Wheel in the ATLAS experiment. NSW detectors will enable the muon system to cope with the increased luminosity of the accelerator, and consequently the large amount of data that will be generated, by improving its performance.

In particular, the first part of the thesis presents the creation of a computer tool that was designed to control the ATLAS Local Trigger Interface (ALTI) and to simulate realistic trigger conditions. ALTI is an important upgrade to the experiment’s Timing, Trigger and Control (TTC) system, which is responsible for the synchronous signal distribution within the LHC detectors and electronic modules.

In the second part of this thesis, a data analysis is performed on tests with NSW small-strip Thin Gap Chamber (sTGC) detectors at the CERN Gamma Irradiation Facility (GIF^{++}). At GIF^{++} the detectors were exposed to a high-energy muon/pion beam ($\leq$ 150 GeV/c) combined with a strong ^{137}Cs gamma irradiation source.

Περίληψη

Η παρούσα διπλωματική εργασία εκπονήθηκε στο πλαίσιο του διατμηματικού μεταπτυχιακού προγράμματος σπουδών: «Φυσική και Τεχνολογικές Εφαρμογές» του Εθνικού Μετσόβιου Πολυτεχνείου σε συνεργασία με το Εθνικό Κέντρο Έρευνας Φυσικών Επιστημών «Δημόκριτος». Πραγματοποιήθηκε εξ ολοκλήρου στο CERN το έτος 2020-2021.

Ο ανιχνευτής ATLAS, μέρος του Μεγάλου Ανδρονίκου Επιταχυντή (LHC) στο CERN, θα υποβληθεί σε μια σειρά αναβαθμίσεων προκειμένου να διατηρήσει την απόδοση του σε υψηλά επίπεδα σε High Luminosity - LHC (HL-LHC) συνθήκες. Στόχος του προγράμματος HL-LHC είναι η βελτίωση της ανίχνευσης σωματιδίων και η δυνατότητα παρατήρησης σπάνιων γεγονότων, αυξάνοντας τον συνολικό αριθμό των συγκρούσεων πρωτονίου-πρωτονίου στον LHC.

Ο σκοπός της παρούσας διπλωματικής εργασίας είναι η μελέτη του συστήματος σκανδαλισμού του αναβαθμισμένου μιονικού φασματόμετρου New Small Wheel στο πείραμα ATLAS. Οι ανιχνευτές NSW θα επιτρέψουν στο σύστημα μιονίων να ανταπεξέλθει στην αυξημένη φωτεινότητα του επιταχυντή, και κατά συνέπεια στον μεγάλο όγκο δεδομένων που θα παραχθεί, βελτιώνοντας την απόδοσή του.

Ειδικότερα, στο πρώτο μέρος της εργασίας παρουσιάζεται η δημιουργία ενός υπολογιστικού εργαλείου που σχεδιάστηκε για να ελέγχει το ATLAS Local Trigger Interface (ALTI) και να προσομοιώνει ρεαλιστικές συνθήκες σκανδαλισμού. Το ALTI αποτελεί μια σημαντική αναβάθμιση του συστήματος χρονισμού, σκανδαλισμού και ελέγχου (TTC) του πειράματος, το οποίο είναι υπεύθυνο για τη σύγχρονη διανομή σημάτων στους LHC ανιχνευτές και τις ηλεκτρονικές μονάδες.

Στο δεύτερο μέρος αυτής της εργασίας, πραγματοποιείται μια ανάλυση δεδομένων από πειράματα σε NSW small strip Thin Gap Chamber (sTGC) ανιχνευτές στο Gamma Radiation Facility (GIF^{++}) του CERN. Στο GIF^{++} οι ανιχνευτές εκτέθηκαν σε μια δέσμη μιονίων/πιονιών υψηλής ενέργειας ($\leq$ 150 GeV/c) σε συνδυασμό με μια ισχυρή πηγή ^{137}Cs ακτινοβολίας γάμμα.

Contents

Page

Chapter 1

The Large Hadron Collider and the ATLAS experiment

In this chapter the world's largest particle accelerator is introduced: the Large Hadron Collider at CERN. Emphasis is laid on the ATLAS experiment with a brief description of all the sub-detector components.

1.1 The Large Hadron Collider

The Large Hadron Collider (LHC) is the world's largest and most powerful particle accelerator, located at the European Organization for Nuclear Research (CERN) in Geneva, Switzerland (Figure 1.1)

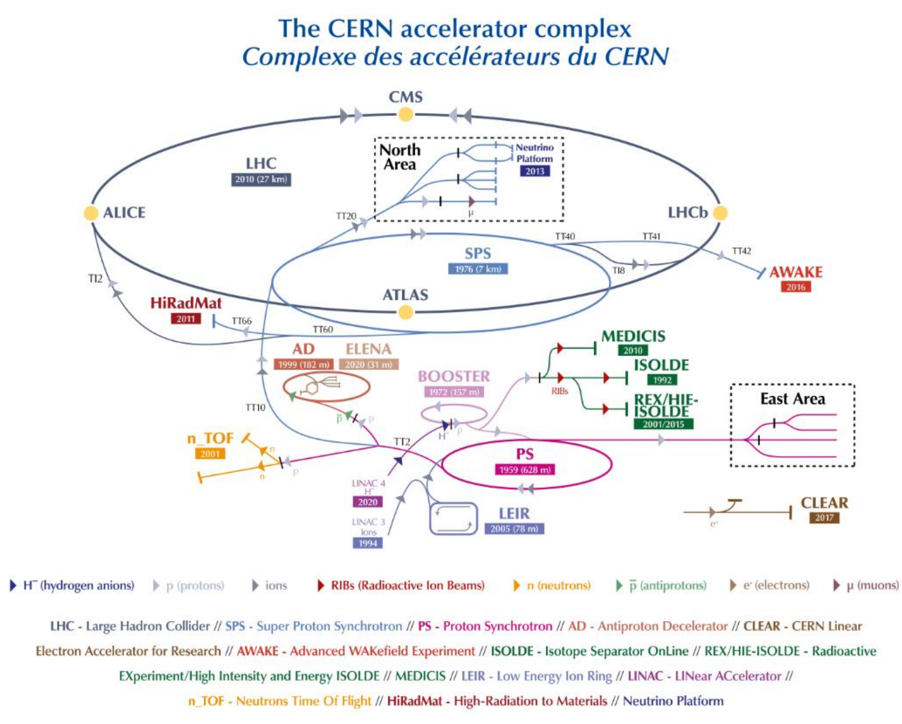

Figure 1.1: The CERN accelerator complex and the LHC. [1]

Approximately 100 m under the French-Swiss border, LHC lies in a circular tunnel (~ circumference of ~ 27 km) extending from the CERN Meyrin site to the foothills of the Jura mountains. It is a successor to the Large Electron–Positron Collider (LEP) (1989-2000) and remains the latest addition to the CERN accelerator complex, being fully operational since September 2008.

There, scientists can reproduce the conditions that existed within a billionth of a second after the Big Bang by accelerating and colliding subatomic particles close to the speed of light. The LHC's goal is to allow the exploration of new physics beyond the Standard Model, to gain a better understanding of current discoveries and even answer some of the fundamental open questions in physics. Particle collisions occur at four interaction points, which correspond to the main underground experiments: ATLAS, CMS, ALICE and LHCb.

1.1.1 LHC particle beams

Before entering the LHC ring, particles undergo a series of accelerations that successively and gradually increase their energy. The first accelerating system in this process is the Linear accelerator 4 (Linac4) and is designed to boost negative hydrogen ions to high energies at 160 MeV. During this process, H^- ions are stripped of their two electrons leaving the nucleus containing one proton. Linac4 injects them to the Proton Synchrotron Booster (PSB) where proton energy is increased to 2 GeV. PSB prepares them to enter the next machine, the Proton Synchrotron (PS) where protons reach energies of 26 GeV. The final stage in particle acceleration, before their injection into LHC, is the Super Proton Synchrotron (SPS) and is used to increase their energy further to 450 GeV.

Inside the accelerator, two particle beams travel in opposite directions around the ring before they eventually collide. The beams are kept in separate parallel beam pipes at ultrahigh vacuum. LHC relies on a superconducting magnet system to create a strong magnetic field that bends and guides them through the ring. The particles within the two beams are grouped in bunches which are focused strongly to a tiny spot near the interaction point to increase the chances of a collision (Figure 1.2). While primarily a proton-proton collider, LHC is capable of accelerating both protons as well as heavy ions in each of its beams. This allows the various LHC experiments to study proton-proton (pp), proton-lead (p-Pb), or lead-lead (Pb-Pb) collisions.

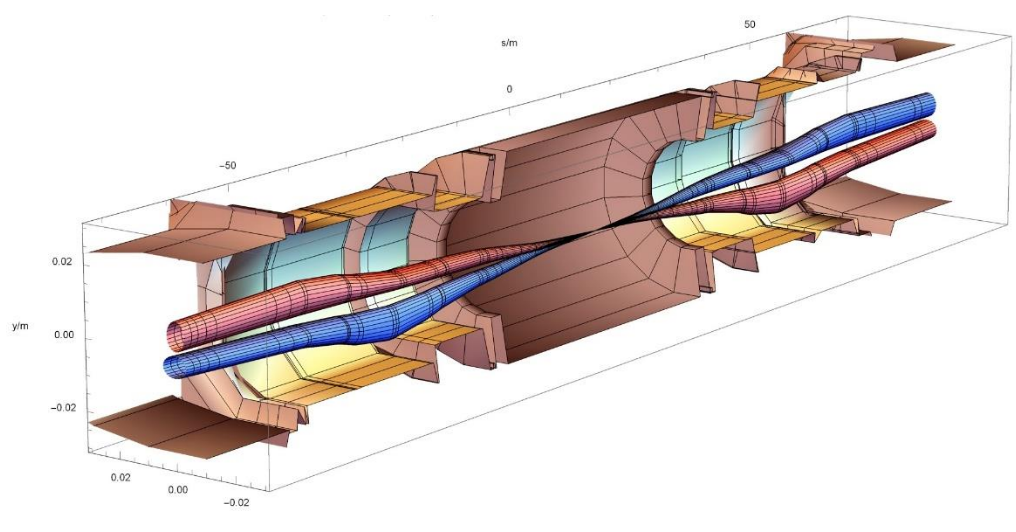

Figure 1.2: Computer visualization of the relative beam sizes in the interaction region at the ALICE experiment. Bunches of Beam 1 move from left to right inside the blue envelope while bunches of Beam 2 travel from right to left inside the red envelope. [2]

The beam structure describes the time distribution of these bunches along one LHC orbit (Figure 1.3). It is comprised of 3564 bunches with $1.15 \cdot 10^{11}$ protons per bunch. The effective number of bunches is 2808 which are delivered at a bunch spacing of 25 ns (or 7.5 m in distance).

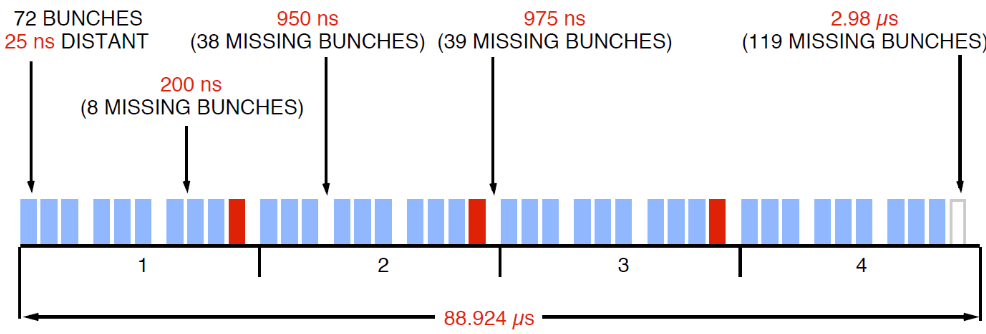

Figure 1.3: The nominal LHC beam structure. [3]

Luminosity

Along with the beam energy, another important parameter for the LHC and an essential indicator of an accelerator's performance is luminosity [4]. It describes the flux density of particle events at the collision points and it is defined by the number of collisions N per time interval for a given cross section σ. A high luminosity can be reached by colliding beams with a high number of protons per beam on a small area with a high frequency. The following relation is used to express luminosity:

$$L = \frac{1}{\sigma} \cdot \frac{dN}{dt}$$

The unit of luminosity is therefore $cm^{-2} \cdot s^{-1}$. A related quantity is integrated luminosity L_{int}, which is the integral of the luminosity with respect to time:

$$L_{int} = \int L \, dt$$

L is dependent on the particle beam parameters, such as beam size and particle flow rate. The instantaneous luminosity of the machine can therefore be expressed in terms of the numbers of particles per colliding bunch, n_1 and n_2, the vertical beam sizes, σ_x and σ_y, the revolution frequency of LHC and the number of bunches N_b:

$$L_{int} = \frac{f \cdot n_1 \cdot n_2 \cdot N_b}{4\pi \cdot \sigma_x \cdot \sigma_y}$$

For $f = 11.3\ kHz$, $n_1 = n_2 = 1.15 \cdot 10^{11}$, $N_b = 2808$ and $\sigma_x = \sigma_y = 16 \cdot 10^{-4}$ c, the nominal LHC Luminosity is calculated at $L \sim = 10^{34} \cdot\ cm^{-2} \cdot s^{-1}$.

1.1.2 LHC experiments

Beam collisions occur at four interaction points where ATLAS, CMS, ALICE and LHCb detectors are installed.

ATLAS and CMS
A Toroidal LHC Apparatus (ATLAS) and the Compact Muon Solenoid (CMS) are two general-purpose detectors at the LHC. They are designed to study many aspects of particle production and decay. Their broad physics programme ranges from precision measurements of the Higgs boson to searching for extra dimensions and new physics beyond the Standard Model. The experiments have similar scientific goals but use different technical solutions and design.

ALICE
ALICE (A Large Ion Collider Experiment) is a detector dedicated to heavy-ion physics at the LHC. It studies the physics of strongly interacting matter at extreme energy densities and very high temperatures, where a phase of matter called quark-gluon plasma forms. In this state of matter quarks and gluons are no longer confined inside hadrons. Such conditions probably existed just after the Big Bang, before particles such as protons and neutrons were formed.

LHCb
The Large Hadron Collider beauty (LHCb) experiment specializes in investigating the slight asymmetry between matter and antimatter that is present in interactions of B-particles. These particles contain a type of quark called the "beauty quark" or "b quark".

1.2 A Toroidal LHC Apparatus

ATLAS is one of the largest detectors ever constructed for particle experiments. Over a billion particle interactions take place in the detector every second, with particles colliding at a center-of-mass energy $\sqrt{s} = 13$ TeV (Run II). It features a cylindrical shape, divided into a barrel region and two end-cap regions. (Figure 1.4).

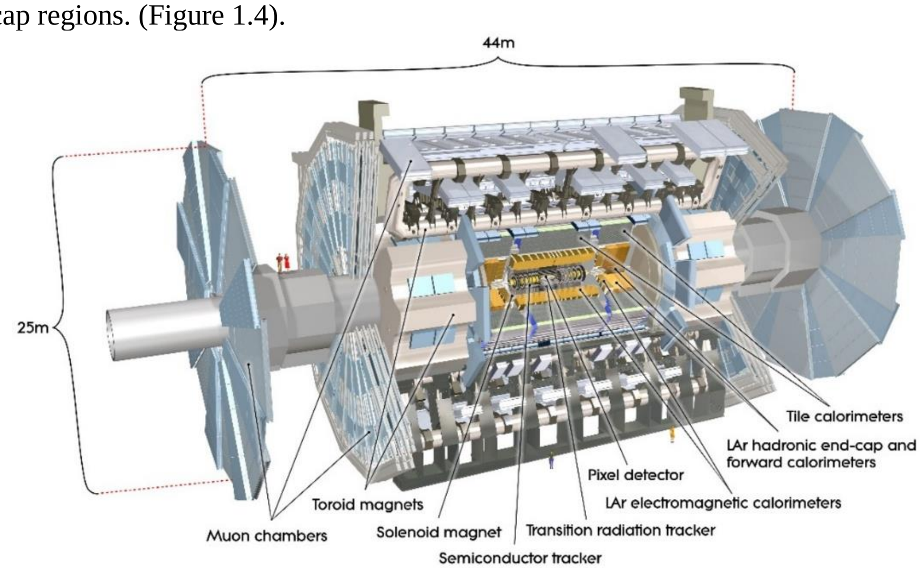

Figure 1.4: Cut-away view of the ATLAS detector and detecting subsystems. The detector is 46 m long, 25 m in diameter and weighs 7000 tones. [5]

The ATLAS detector consists of six different detecting subsystems wrapped concentrically in layers around the collision point. The multi-layer detection system records the trajectory, momentum and energy of traversing particles, allowing them to be individually identified and measured as they leave different traces in each layer of the detector (Figure 1.5). In the following sections, the different ATLAS subdetectors are presented and discussed.

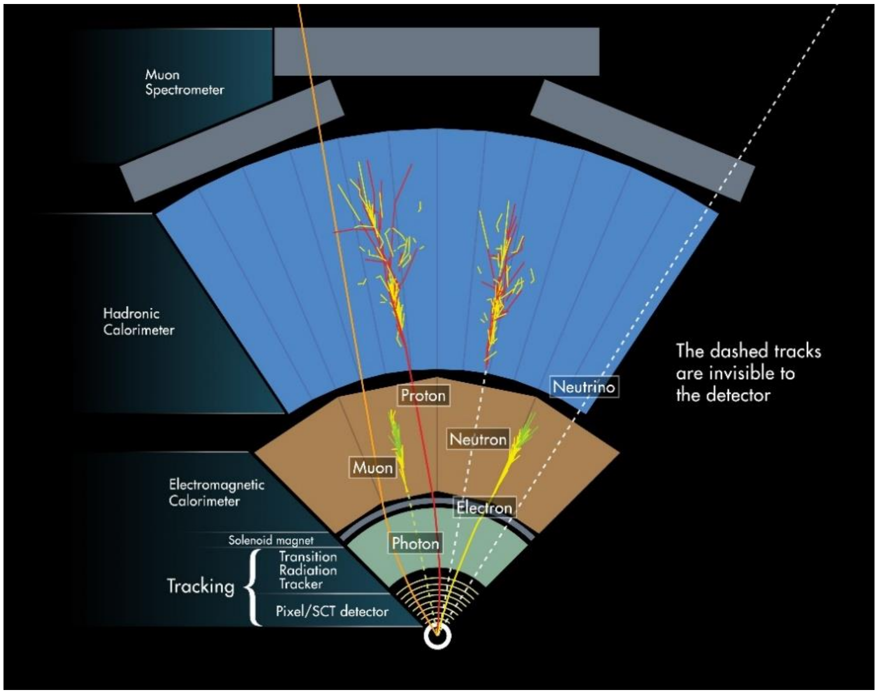

Figure 1.5: Diagram of particle paths in the ATLAS detector. [6]

Coordinate system

The ATLAS experiment uses a right-handed coordinate system with the origin of the system at the nominal interaction point (IP) in the center of the detector. The z-axis is along the beam pipe (pointing to Geneva) and is perpendicular to the xy plane, referred to as the transverse plane. The positive x-axis points from the IP to the center of the LHC ring and the positive y-axis is pointing upwards. The azimuthal angle φ is measured around the z-axis.

In particle collider physics, we additionally utilize the polar angle θ, the angle with respect to the beam axis, to characterize the detected particle. It can be expressed in terms of the pseudorapidity variable (η) which is defined by the following relation:

$$\eta = -ln\left[\tan\left(\frac{\theta}{2}\right)\right]$$

with values between (−∞, ∞). For a particle with high θ, the parameter η has lower values (barrel region) whereas for θ closer to the beam line η goes to infinity (end-cap regions).

Experimentally, pseudorapidity can be easily measured by knowing only the polar emission angles of the produced particles. The concept of pseudorapidity is often preferred because rapidity differences are Lorentz invariant under boosts along the beam direction and hence particle production can be considered constant as a function of rapidity. The transversal momentum p_T and energy E_T are also defined in terms of the polar angle as $p_T = p \cdot sin\theta$ and $E_T = p \cdot sin\theta$, respectively.

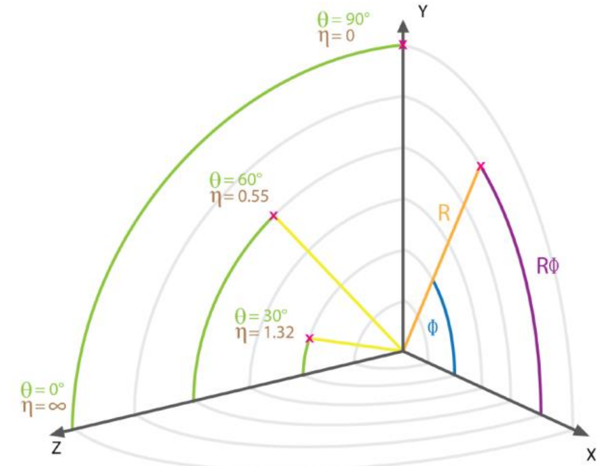

Figure 1.6 Geometric relation of between pseudorapidity η, the azimuthal angle φ and the polar angle θ. [7]

1.2.1 Inner Detector

Closest to the interaction point, the inner detector is the first part of the ATLAS detection system and measures the direction, momentum, and charge of electrically-charged particles produced in each p-p collision. It consists of three subsystems: the Pixel Detector, the Semiconductor Tracker **(**SCT) and the Transition Radiation Tracker (TRT).

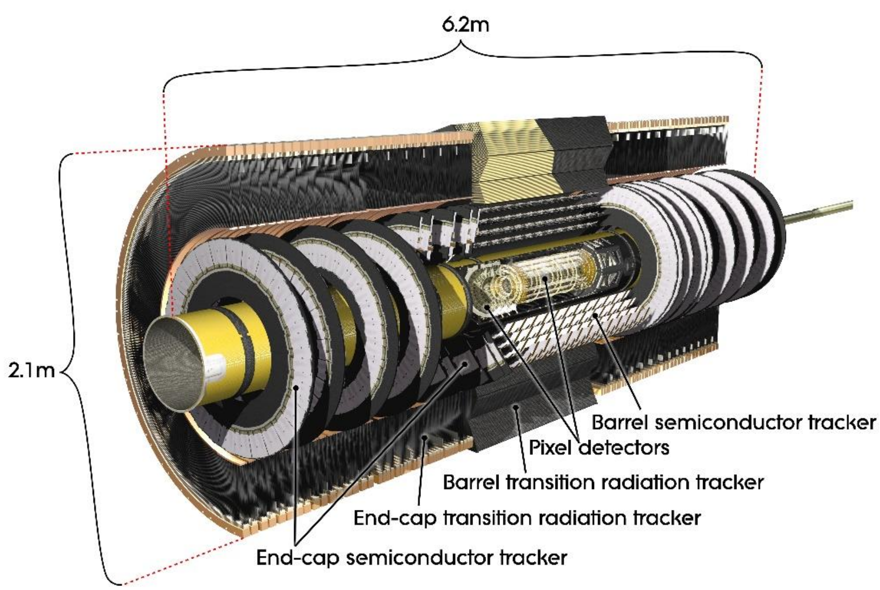

Figure 1.7: The inner detector at the ATLAS experiment. It extends to a radius of 1.1 m and is 6.2 m in length along the beam pipe, providing tracking measurements in the pseudorapidity range |η| < 2.5. [8]

The entire inner detector is immersed in a 2T magnetic field parallel to the beam axis, created by a cylindrical superconducting coil, which causes charged particles to curve. The direction of the curve reveals the particle's charge and the degree of curvature its momentum. The starting points of a particle's track can additionally provide information on particle identification.

1.2.2 Calorimeters

Following the inner detector, the calorimeter detector system is designed to detect particles that interact through electromagnetic and strong interactions with matter. It consists of alternating layers of an "absorbing" high-density material that degrades the energy of incoming particles and an "active" medium that measures their energy deposition as they pass through the detector (Figure 1.8).

The ATLAS calorimetry system is divided into two main categories:

- **the Liquid Argon calorimeter (LAr):** electromagnetic calorimeter measuring mainly the energy of electrons and photons as they interact with matter. It features layers of metal absorbers (either tungsten, copper or lead) with liquid-argon as active material between them.

- **the Tile Hadronic Calorimeter (TileCal)**: hadronic calorimeter that samples the energy of hadrons as they interact with atomic nuclei. It is made of alternating layers of steel absorbers and scintillating tiles.

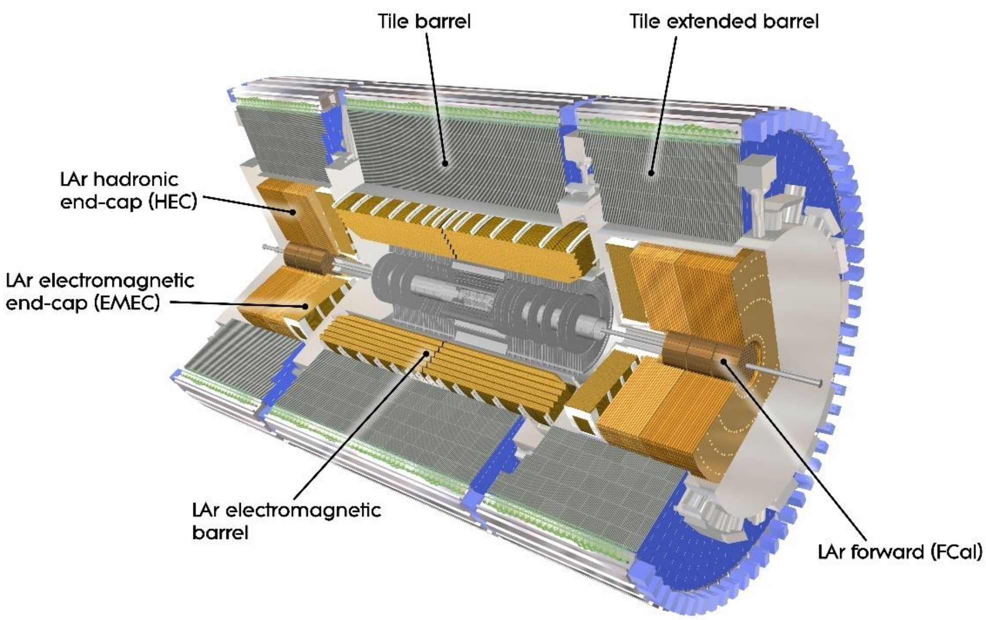

Figure 1.8: The calorimeter system at the ATLAS experiment. LAr and TileCal are illustrated along with their segmentation in the barrel and end-caps regions, providing coverage in $|\eta| < 4.9$. [9]

The energy signature of each particle is different and for this reason most particles, when they reach the calorimeters along with the information that the Inner Detector provides, can be identified and their properties measured.

1.2.3 Muon Spectrometer

Located at the outermost region of the ATLAS detector, the muon spectrometer measures the momenta of charged particles that exit the calorimeters. Among them are the muons, which are minimum ionizing particles and pass through every other layer of the ATLAS detector undetected. This requires a detector system specifically designed for their identification and standalone measurement over a wide range of transverse momentum, pseudorapidity and azimuthal angle.

The muon spectrometer is made up of 4,000 individual muon chambers, installed both in the barrel and the end-cap regions, that employ four different gas-filled detector technologies (Figure 1.9).

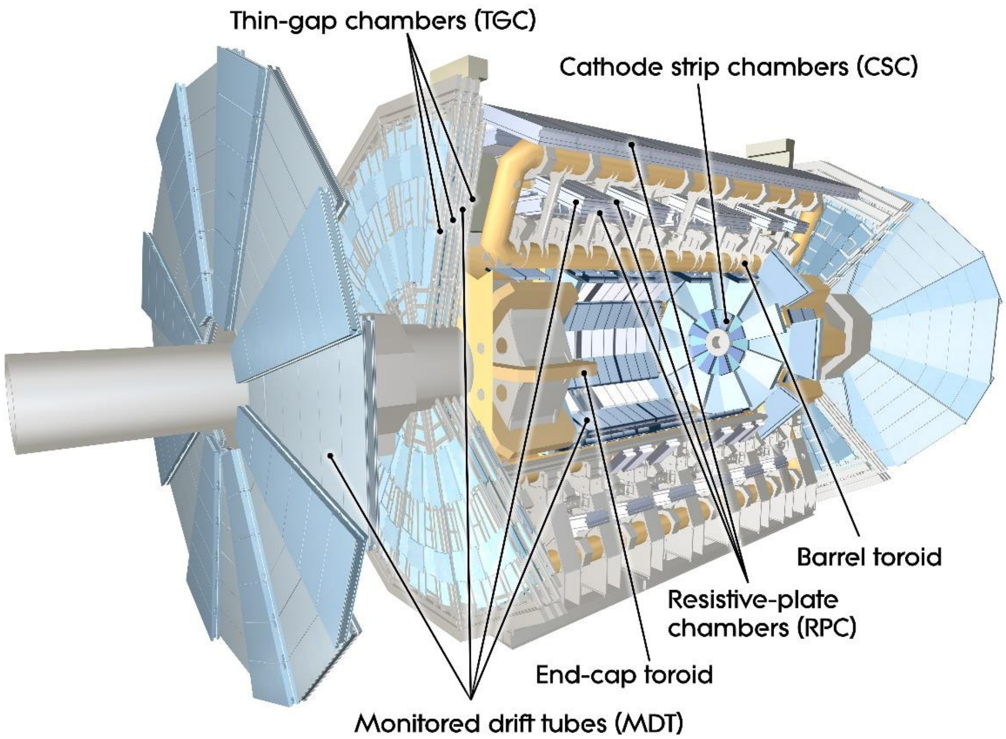

Figure 1.9: The muon spectrometer at the ATLAS experiment. [10]

The muon chambers have a rectangular shape in the barrel region and are arranged in three concentric stations around the beam axis. They occupy a space of 4.5 m in length and 11 m in radius. In the end-caps, the muon chambers have a trapezoidal shape and are mounted on three different wheels. Each wheel is installed perpendicular to the beam pipe at a distance of 7 m, 13 m and 23 m from the interaction point, on both sides of the detector (Figure 1.10). Table 1.1 summarizes the main detector technologies of the muon spectrometer and their properties.

Detector technology	Region	Function	|η| coverage
Thin Gap Chambers (TGC)	End-caps	Triggering, 2nd coordinate measurement	1.05 < |η| <2.7
Resistive Plate Chambers (RPC)	Barrel	Triggering, 2nd coordinate measurement	|η| < 1.05
Monitored Drift Tubes (MDT)	End-caps, Barrel	Precision tracking	|η| < 2.7
Cathode Strip Chambers (CSC)	End-caps	Precision tracking	2.0 < |η| < 2.7

Table 1.1: Detector technologies of the current muon spectrometer and their |η| coverage.

The position of each detector is optimized to provide good hermeticity and optimal momentum resolution. The design goal was to measure the transverse momentum of $p_T = 100\ GeV$ muons with 3% accuracy and of $p_T = 1\ TeV$ muons with 10% accuracy.

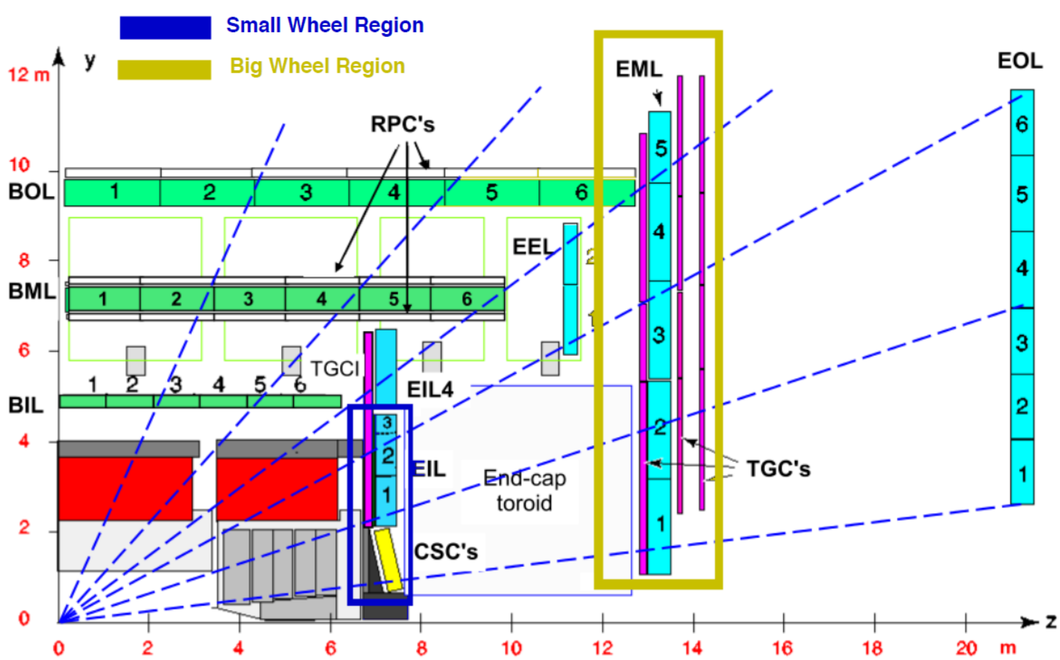

Figure 1.10: Cross-section of the muon system in a plane containing the beam axis. Each detector technology along with the three muon wheels are depicted. [11]

1.2.4 Magnet System

The ATLAS magnet system bends the trajectories of charged particles around the various layers of the detector's subsystems, allowing them to measure their momentum and charge. It contains two types of superconducting magnets (Figure 1.11):

- **The Central Solenoid (CS) magnet**
  It surrounds the inner detector, sharing a cryostat with the Lar calorimeter. At the CS, a single layer coil is wound with an aluminum stabilized niobium-titanium conductor. It provides a 2 Tesla axial magnetic field parallel to the beam direction and operates at 7.73 kA nominal current. It is 5.6 m long, 2.56 m in outer diameter, 4.5 cm in thickness and weighs over 5 tones.

- **The Toroid magnets**
  Located outside of the calorimeters, the three air-cored toroid magnets provide a magnetic field of up to 4 T. It is perpendicular to that of the central solenoid magnet and created by eight superconducting coils in the barrel and two rotors with eight coils each in end-cap region, both symmetrically positioned around the beam axis.

  The barrel toroid is the largest toroidal magnet ever constructed with a total length of 25.3 m. It uses over 56 km of superconducting wire, has a 20.1 m outer diameter and weighs about 830 tones. The end-cap toroid magnets extend the magnetic field, which reaches particles leaving the detector close to the beam pipe. Each end-cap is 5.0 m in axial length, has a 10.7 m in diameter and weighs 240 tones.

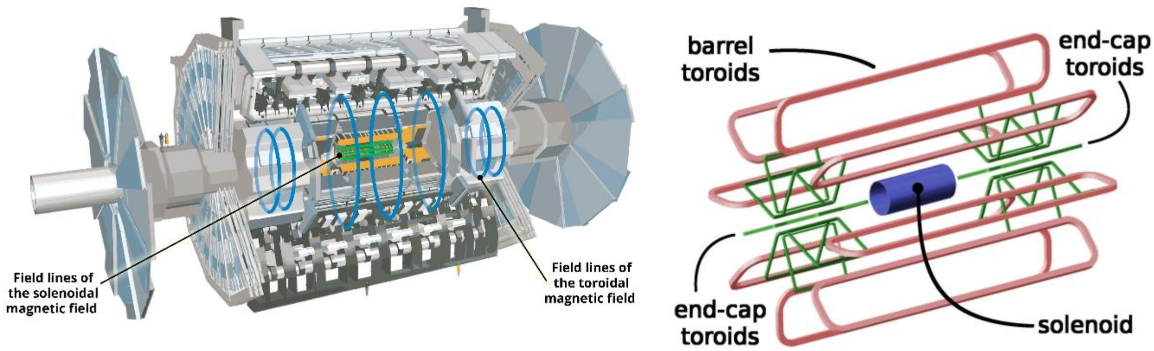

(a) (b)

Figure 1.11: (a) The magnet system at the ATLAS experiment generates a magnetic field in an enormous volume and is fully integrated with the ATLAS subdetectors. (b) The Central Solenoid and Toroid magnets with respect to the beam axis. The CS and the Toroid magnets cover a pseudorapidity range of $|\eta| < 1.4$ and $1.4 < |\eta| < 1.6$, respectively. [12, 13]

The magnet system is operated at a temperature of < 4.5 K (-269°C) and as a result the majority of the accelerator is connected to a distribution system of liquid helium that provides cooling.

1.2.5 Trigger and Data-Acquisition (TDAQ) system

The ATLAS trigger and data-acquisition (TDAQ) system is based on three levels of real-time event selection (Figure 1.12). It is designed to collect data from the detector systems, digitally convert and convey them to CERN permanent data storage for offline analysis [14].

At the LHC nominal bunch-crossing rate of 40 MHz, an average of 20 proton-proton collisions is observed per bunch crossing (BC). The selective trigger system identifies and accepts among them events with interesting characteristics, ultimately reducing the event rate to ~100 Hz. This is achieved by applying selection criteria in each level and refining the decisions made at the previous one.

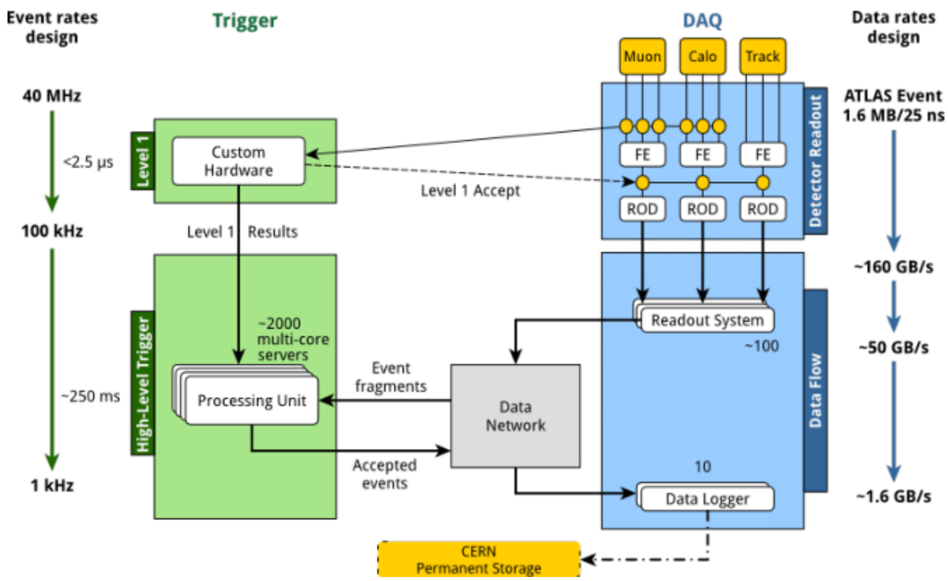

Figure 1.12: Schematic of the ATLAS trigger and data acquisition system for Run 2. [15]

The triggering system utilizes a multi-level approach [16, 17]:

- A level composed of custom-made electronics responsible for the initial event selection after processing input signals from the calorimeter and muon detectors. This level is called Level-1 trigger (LVL1), where event rate is reduced to 100 kHz in less than 2.5 μs.

- A set of software-based levels with access to the detector data at full granularity. It is comprised of Level-2 and Level-3, together called the High-Level Trigger (HLT).

  Level-2
  Event selection is based only on a subset of event data in the Regions of Interest (RoI), geometrical regions in η x φ plane which contain the signature of a physics object, identified by LVL1. Event rate is reduced to 1 kHz and latency is calculated at ~ 40 ms.

  Level-3 (Event Filter)
  Analyzes the events selected by LVL2, using offline analysis procedures, and sends the accepted ones to the Sub-Farm Output (SFO) for subsequent offline analysis. There, the events are streamed into local data files, which are asynchronously moved to the permanent storage. Event rate is reduced to 200 Hz, with an average event processing time of approximately 4 s.

Read out and data flow
After an event is accepted by LVL1, data related to it are transferred from the detector front-end electronics systems to the Read-Out Drivers (RODs) and the Read-Out System (ROS). They are buffered there either until the event is requested by the HLT. At the HLT, event selection based on data from RoI and full event-building is performed. Accepted events are sent to the Data Collection Network (DCN) for transfer to permanent data storage via the SFO server.

Chapter 2

The High Luminosity Large Hadron Collider (HL-LHC) project

This chapter focuses on the High Luminosity LHC concept of upgrades at the LHC and particularly on the ATLAS experiment and the New Small Wheel Upgrade. Additionally, the electronic upgrades and detector technologies that have been deployed by the NSW are described.

2.1 LHC towards the High Luminosity era

Following the successful discovery of the Higgs particle during the first LHC run, CERN plans the full exploitation of the LHC in order to further increase its discovery potential until 2040 or beyond. The High-Luminosity Large Hadron Collider (HL-LHC) will accomplish this by bringing an upgraded version of the LHC.

It aims to increase the total number of proton-proton collisions and operate at a higher luminosity, ultimately reaching LHC peak luminosity ten times beyond the nominal value. A more powerful LHC will improve particle detection and enable the observation of rare processes that occur below the current sensitivity level. This will allow physicists to study known mechanisms in greater detail and increase the potential for discovering new physics beyond the Standard Model.

The path to High Luminosity will be gradual and flexible to accommodate the evolution of LHC operational parameters and indications of new physics signals (Figure 2.1). It includes two phases, which correspond to two long technical shutdowns of the LHC:

- Phase 1: (2018-2022)
  Luminosity up to $L = 2 \times 10^{34} cm^{-2} s^{-1}$ (~ 80 collisions/bunch crossing),
  Integrated Luminosity: $L_{int} = 350\ fb^{-1}$ at Run 3.

- Phase 2: (2026-2027)
  Luminosity up to $L = 5\ to\ 7.5 \times 10^{34} cm^{-2} s^{-1}$ (~ 200 collisions/bunch crossing),
  Integrated Luminosity: $L_{int} = 3000 - 4000\ fb^{-1}$ at Run 4.

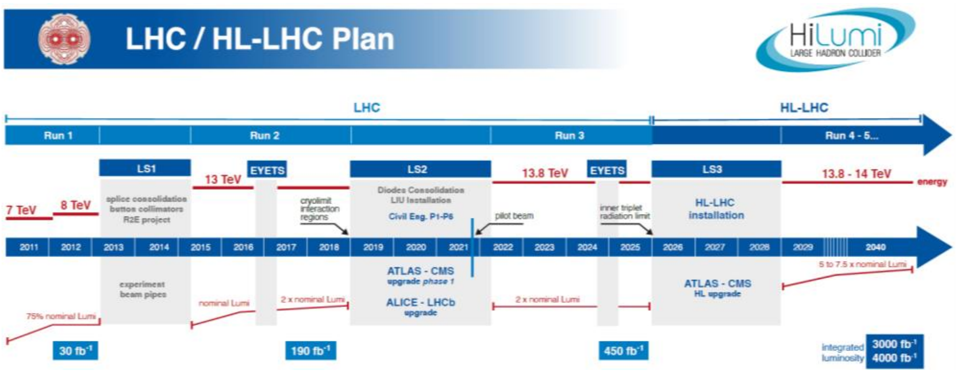

Figure 2.1: Timeline for the HL-LHC plan (February 2022). [18]

In order to maintain high physics performance and withstand the increased particle rate, the experiments are preparing a series of upgrades including the installation of updated or innovative detector technologies, trigger electronics and data acquisition systems. These upgrades are significant in terms of handling expected radiation levels, trigger rates at low-p_T thresholds, pile-up mitigation and detector occupancy.

2.2 Phase-I ATLAS upgrades

The ATLAS Phase-I upgrade will take place during Long Shutdown 2 (LS2) and will impact on three areas of the ATLAS detector: the Liquid Argon (LAr) calorimeter, the muon detectors in the end-cap region and the TDAQ system. More information can be found on Ref. [11, 19, 20].

Liquid Argon Calorimeter

New trigger electronics boards will be installed in the front-end (Trigger Digitizer Boards) and back-end (Digital Processing Boards) region of the calorimeter. The objective of these upgrades is to refine current trigger towers and increase the granularity from $\Delta\eta\times\Delta\varphi$ = 0.1×0.1 to $\Delta\eta\times\Delta\varphi$ = 0.025×0.1 (Figure 2.2).

Additionally, the Level-1 LAr calorimeter trigger system (L1Calo) will be equipped with the new Feature EXtractor boards (FEXs). This will improve the trigger energy resolution and efficiency for selecting electrons, photons, τ leptons, jets and missing transverse momentum E_T^{miss}, while enhancing discrimination against background and fake triggers.

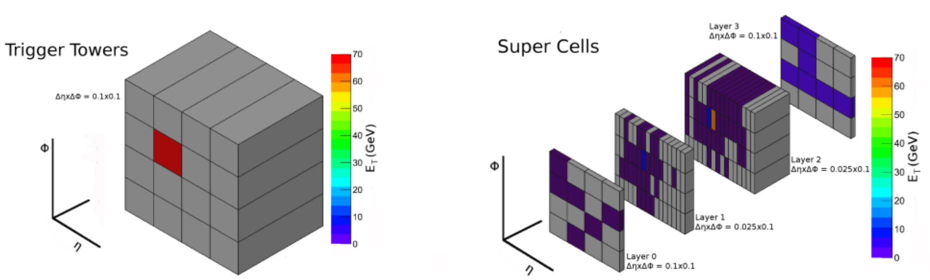

Figure 2.2: An electron (with E_T = 70 GeV) as seen by the existing Level-1 Calorimeter trigger electronics (left) and by the proposed upgraded trigger electronics (right). [19]

Muon detectors in the end-cap region

At the ATLAS muon spectrometer, the current inner station of the experiment's muon end-cap system called Small Wheels will be replaced by New Small Wheels. The New Small Wheels aim to:

- Improve tracking efficiency in the high-rate environment (up to 15 $kHz/\ cm^2$).
- Reduce fake triggers from background hits (Figure 2.3). Currently 90% of muon trigger rate in the end-cap region (1.3 < |η| < 2.7) is caused by noise or accidental coincidences.
- Provide spatial resolution at 100 μm and angular resolution < 1 mrad at the muon Level-1 Trigger system.

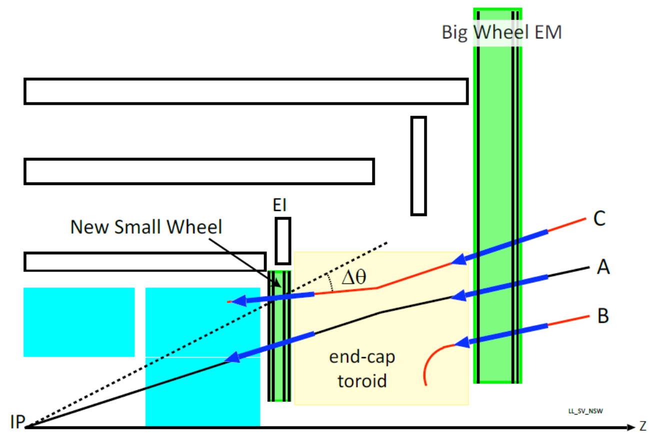

Figure 2.3: Track selection by New Small Wheel. Track A is accepted, while track B (producing hits only in the Big Wheel) and track C (not pointing to the interaction point) would be rejected. [11]

The New Small Wheel will be comprised of two gaseous detector technologies: the MicroMegas (MM) detectors that provide precision tracking capabilities, and the small-strip Thin Gap Chambers (sTGC), primarily deployed for triggering.

Trigger and data Acquisition (TDAQ) system

The ATLAS TDAQ system (Figure 2.4) will upgrade in order to handle data taking and to ensure high detector performance, considering the increased number of collisions per bunch crossing. Key parts of the upgrade process are listed below:

- New feature extraction processors for the calorimeter (e/j FEX) will make full use of the finer granularity upgrade at the Level-1 Calorimeter Trigger system.
- Muon trigger processors (Sector Logic) will be incorporated to reduce trigger rate in the end-cap region.
- A topological processor (L1Topo) will compute kinematic quantities and relations among multiple Level-1 trigger objects, such as angular distances or invariant masses.
- The Muon to Central Trigger Processor Interface (MuCTPI) will combine the muon candidate counts from the Barrel and the end-cap regions and manage muon data transfers to the L1Topo processor.

- The new readout system will be based on a Front-End Link Interface Exchange (FELIX) system. It is designed to act as a data router, by receiving data from the detector front-end electronics via links and multiplexing this data on to a network built with commodity switching technology. This will allow a single hardware to handle distribution of clock, trigger signals, configuration and monitoring of the detectors, readout and slow control data.

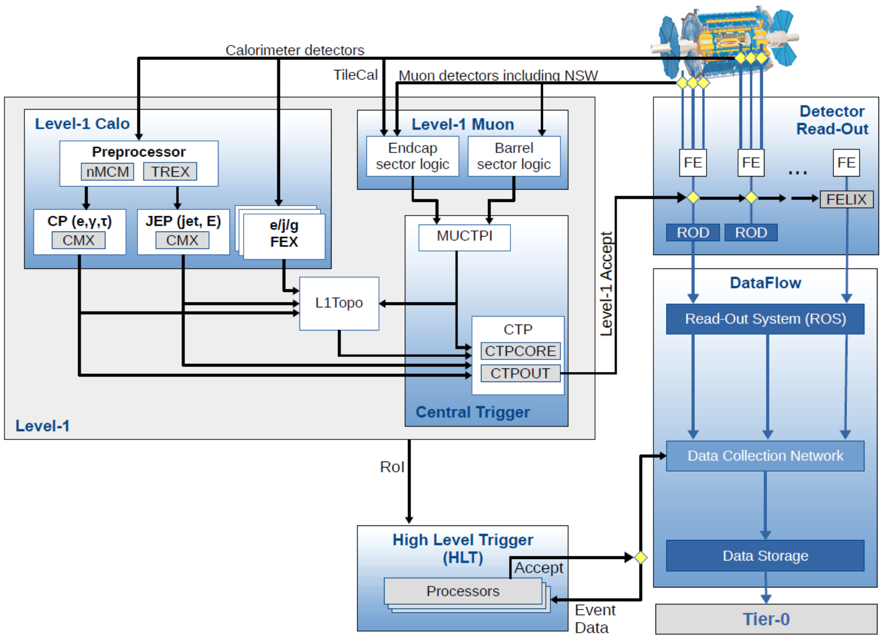

Figure 2.4: Trigger and Data Acquisition system Phase-I upgrades. [21]

2.2.1 NSW detector requirements

The New Small Wheel detectors must maintain excellent performance in terms of efficiency, resolution and background rejection for all the physics objects used in data analysis during the HL-LHC era.

Precision tracking performance

The main requirement on the NSW detectors for the precision tracking performance is to measure the transverse momentum of p_T =1 TeV passing muons with a precision of 10% in the full pseudorapidity coverage area of the Small Wheel (up to $|\eta|$ = 2.7). Additional important requirements are the following:

- Track segment reconstruction with a position resolution to be better than 50 μm in the r-z plane.
- Measurement of the second coordinate with a resolution of 1–2 mm.
- Efficiency at segment finding to exceed 97% for muons with p_T >10 GeV (current efficiency).
- Efficiencies and resolutions should not degrade at very high momenta (due to δ rays, showers etc).

Trigger selection

For current trigger selection, the presence of unexpectedly high rates of fake triggers in the end-cap region has been observed. Figure 2.5 depicts the η distribution of muon candidates selected by the ATLAS Level-1 trigger with p_T > 10 GeV. The distribution of those candidates that indeed have an offline reconstructed muon track is also shown, along with the reconstructed muons with p_T > 10 GeV. The majority (>80%) of the muon trigger rate is from the end-caps (η>1) and is not reconstructible offline.

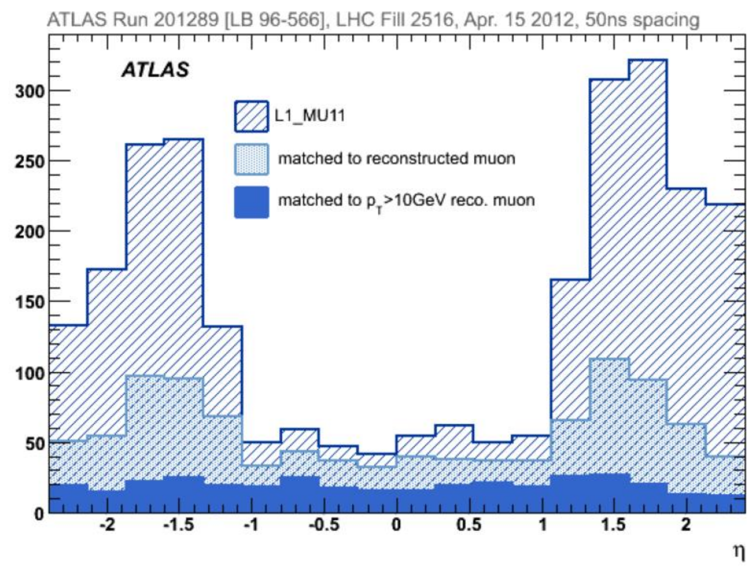

Figure 2.5: η distribution of Level-1 muon signal (p_T > 10 GeV) (L1_MU11). [11]

In order to study the effect of the luminosity increase on the trigger rate, simulations were performed for the Level-1 trigger selections. In these simulations the expected Level-1 muon rate for the present system was compared to the upgraded system after the NSW installation at $\sqrt{s} = 14\,TeV$, $L = 3 \times 10^{34} cm^{-2} s^{-1}$ and 25 ns bunch spacing. To meet the new expectations, the NSW must reduce the muon Level-1 trigger rate to ~20 kHz for muons with p_T > 20 GeV and have the following requirements:

- Data segment delivery to the NSW Sector Logic must happen at a fixed latency, within 43 BC (1075 ns) from each particle collision.
- Granularity of track segments should exceed Δη x Δφ = 0.04 x 0.04 to match the current muon trigger system.
- The online track segment reconstruction in the full coverage of the detector (1.3 < η < 2.5) should have a high efficiency (> 95%).
- The angular trajectory resolution should be better than 1 mrad (RMS) to suppress background signals.

2.2.2 NSW detector technologies and layout

The geometry of the muon spectrometer will remain the same, while the current detector technologies such as Monitored Drift Tubes (MDT), Cathode Strips (CSC) and Thin Gap Chambers (TGC) will be replaced by two types of innovative gaseous detectors: the small strip Thin Gap chambers (sTGC) and the MicroMegas (MM) detectors. Both detectors have excellent timing and spatial coordinate specification, capable of operating in the high particle rate environment of the HL-LHC. In addition, they will complement each other: the sTGC detectors will contribute to the off-line track reconstruction and the MM detectors will contribute to the trigger scheme. A detailed description on the NSW detector technologies and layout can be found on Ref. [11].

small-strip Thin Gap Chambers (sTGC)

sTGC are multiwire ionization chambers that will be deployed as the main triggering detector by the NSW. They measure muon trajectories with angular resolution < 1 mrad and a response time within 1 μs, given their single bunch crossing identification capability.

A wire plane, constructed with 50 μm diameter gold-coated tungsten wires spaced at 1.8 mm, is laid between two resistive cathode planes at a distance of 1.4 mm from the wire plane (Figure 2.6(a)). The parallel cathode planes are made of a graphite-epoxy mixture, with a typical surface resistivity of 100 kΩ/□, sprayed on a 100 μm thick G-10 plane. They are divided into 3.2 mm pitch strips on the one side, that are perpendicular to the wires, and into large rectangular pads on the other side. Pads are placed on a 1.6 mm thick printed circuit board (PCB) with the shielding ground on the opposite side.

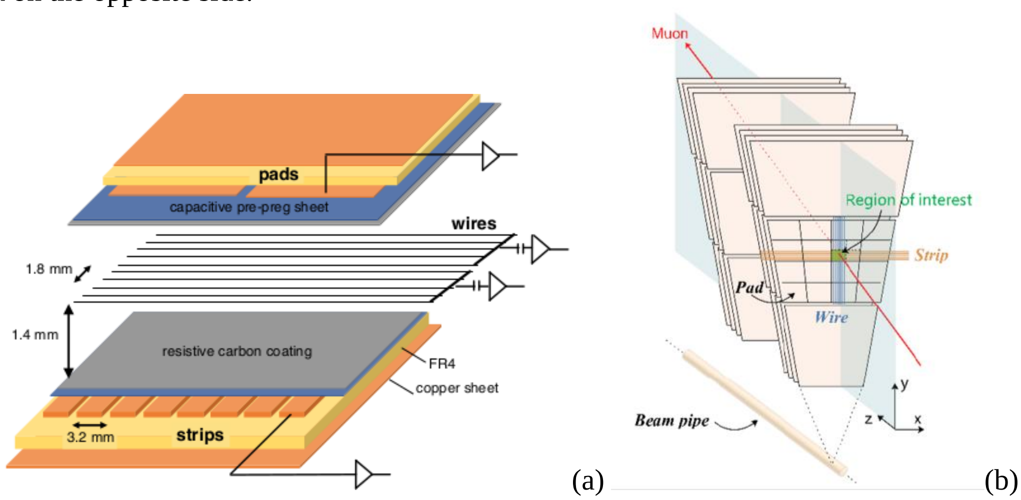

Figure 2.6: (a) Structure of sTGC detectors (b) Orientation of sTGC wire, strip and pad readout electrodes in an NSW sector. Pads on different layers are staggered in the direction orthogonal to the strips. [22, 23]

Pads are used to produce a 3-out-of-4 coincidence in each sTGC quadruplet to identify muon tracks roughly pointing to the interaction point. They define which strips need to be readout to obtain a precise measurement in the bending coordinate (region of interest), for the online event selection (Figure 2.6(b)). Strips and wires are used for precision in muon track reconstruction (η direction). Charge clusters formed at strips are used to calculate a centroid in each quadruplet (pivot and confirm) and create a track segment.

The sTGC operational gas is a mixture of CO_2 and n-pentane (C_5H_{12}) with a ratio of 55:45 at one atmospheric pressure and a voltage of 2.8 kV.

Micro-MEsh Gaseous Structure (MM) detectors

Micromegas detectors are parallel plate detectors that will be used by the NSW as the main track detection mechanism. They provide spatial resolution of < 100 μm independent of particle incidence angle and excellent high-rate capability due to small gas amplification region and small space charge effects.

MM detectors consist of a planar (drift) electrode, a gas gap of 5 mm thickness acting as conversion and drift region, and a thin metallic mesh at 128 μm distance from the readout electrode, creating the amplification region (Figure 2.7). The 17 μm thick Cu readout electrodes are placed on a 0.5 mm PCB board with a 64 μm insulator directly above them. A spark protection system is installed by adding a layer of 0.425 mm pitch resistive strips on top of the insulator. The metallic mess is supported by 128 μm high pillars that are placed on top of the resistive strips.

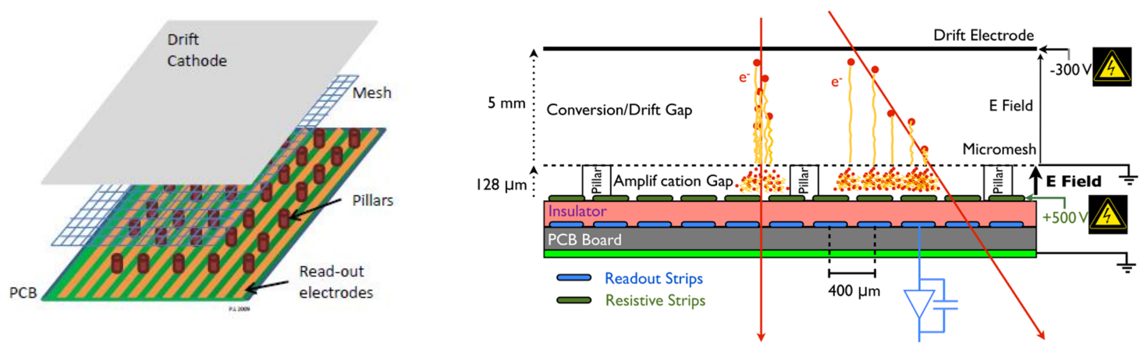

Figure 2.7: Structure (left) and operating principle (right) of the MM detector. [11, 24]

When a charged particle traverses the drift space, it ionizes the Ar:CO_2 gas causing electrons to be liberated by the ionization process and drift towards the micromesh. The electric field in the amplification region is 50-100 times stronger than the drift field and, as a result, the mesh is transparent to more than 95% of the electrons. An electron avalanche takes place in the amplification region (in < 1 ns), immediately above the readout electrode, resulting in a fast pulse of electrons on the readout strip. Ions produced in the avalanche process move in the opposite direction of the electrons, back to the amplification mesh. It is the fast evacuation of the positive ions at < 100 ns which makes the MM particularly suited to operate at very high particle fluxes.

Layout

In order to ensure compatibility with the existing tracking detectors and the end-cap alignment system, the New Small Wheel layout follows the design of the current Small Wheels. Each wheel will consist of 16 detector planes (sectors), of which eight large and eight small in size. The small sectors will be facing the interaction point (IP) while the large sectors are closer to the confirm point (Figure 2.8).

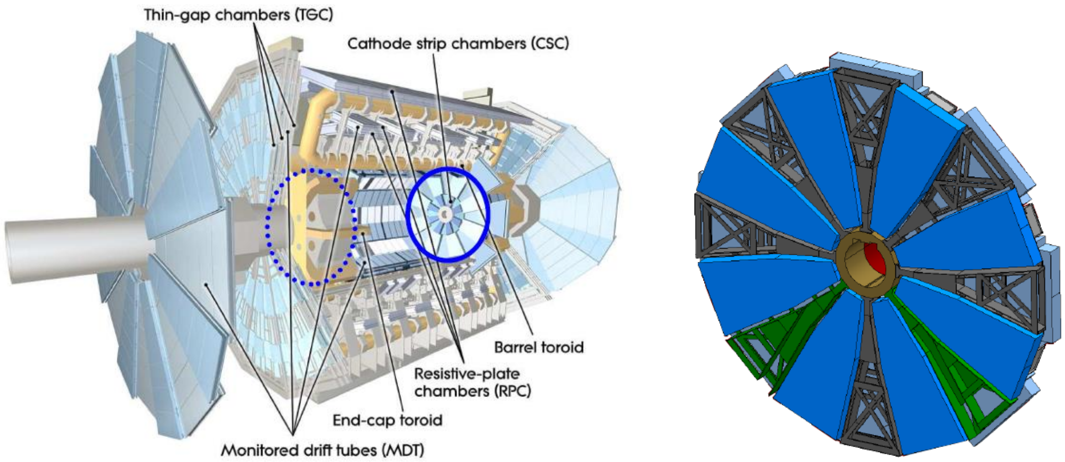

Figure 2.8: Location (left) and overall layout of the New Small Wheel, facing the IP side (right). [25]

Sectors are comprised of two sTGC wedges and two MM wedges, each of them providing four active layers of individual detector technology in the z direction, covering a full sector in the r-φ plane (Figure 2.9). Each sTGC and MM multiplet is radially divided into three and two modules, respectively.

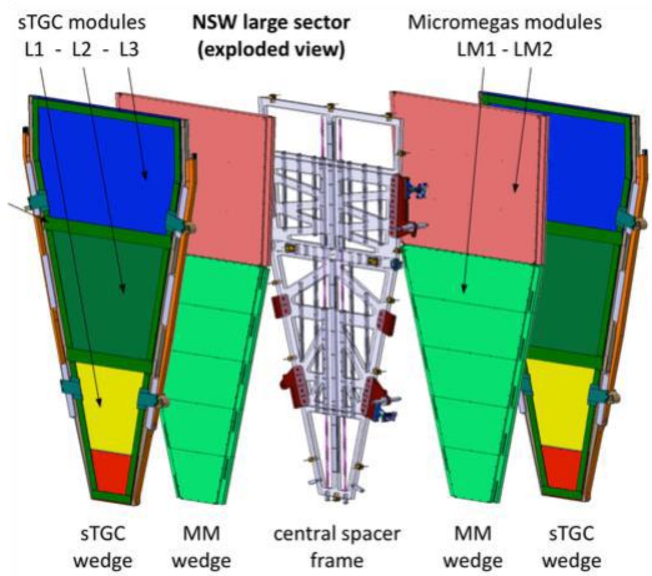

Figure 2.9: Schematic of layers of sTGC and MM detector technology in a NSW sector. [26]

The detectors are aligned in the following sequence: sTGC-MM-MM-sTGC in order to maximize the distance between the sTGC detector multilayers and improve the accuracy of online track hit reconstruction. Support is provided by a central spacer which in turn is mounted on a JD shielding that covers the full extent of the detector wheel with a cylindrical extension (plug) around the beam pipe at the inner radius.

2.2.3 NSW electronics and Data Acquisition (DAQ) dataflow

The NSW trigger system is based on track segments produced online by the sTGC and MM detectors. The NSW trigger electronics and DAQ dataflow includes 128 detectors and ~2.4 million readout channels (Figure 2.10). Separate trigger, data readout and configuration/monitoring paths for both detectors are defined. The entire electronics chain is divided into two sections: on-detector electronics and off-detector electronics, common to both sTGC and MM detectors, deployed in the underground service area.

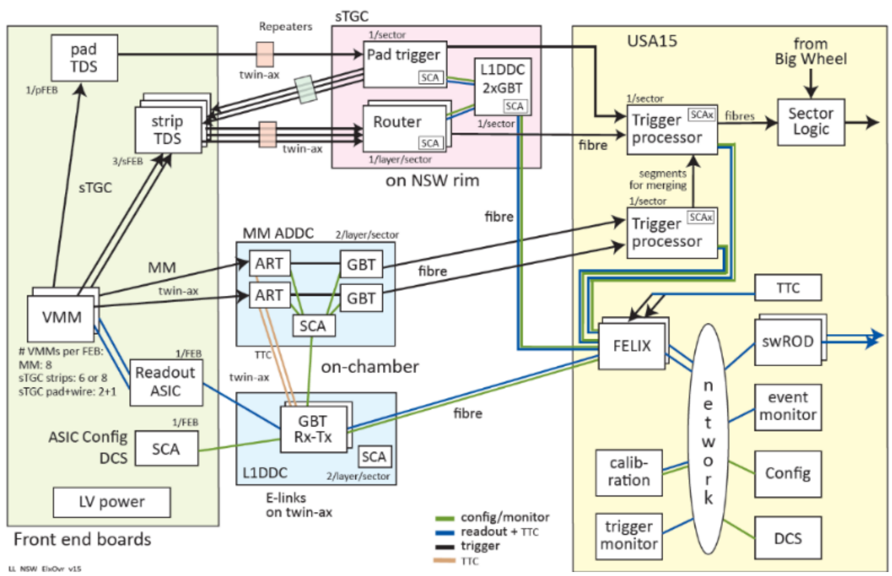

Figure 2.10: Schematic of NSW trigger and DAQ electronics. [27]

On detector electronics include the Front-End Boards (FEB), electronic cards with radiation-tolerant Application Specific Integrated Circuits (ASICs) that are responsible for conveying data and trigger information from the NSW detectors to the rest of the electronics. They are connected to Level-1 Data Driver Cards (L1DDC) and ART Data Driver Cards (ADDC), for the sTGC and the MM detectors respectively. These cards aggregate and transmit the Level-1 data (time, charge and strip address corresponding to a single hit) from multiple front-end boards to FELIX.

Off detector electronics, on the other hand, include a set of high-throughput Back-End electronics such as the sTGC Rim Crate (hosts Pad Trigger Board, rim L1DDCs, Router Board), Trigger Processor, Sector Logic, ALTI, FELIX) and Services (Read Out Drivers (ROD), Detector Control System (DCS) etc.). Communication between the electronics is achieved via mini–Serial Attached Small Computer System Interface (SAS SCSI) cables and optical fibers.

sTGC trigger system

At each bunch crossing, the sTGC trigger electronics find local tracks that point to the outer muon station (Big Wheel) to corroborate its coincidences. This happens at the sTGC FEB which host four types of front-end ASICs (Figure 2.11):

- The VMM is the first FEB ASIC that detects raw pad, strip and wire signals. It provides measurement, amplification, discrimination and the fast digitization of charge and timing information from 64 detector channels.
- The Readout Controller (ROC) interfaces up to 8 VMMs and aggregates readout data packets. It also handles the decoding and distribution of TTC signals to the VMMs, used for the synchronization of the readout and trigger electronics.
- The Trigger Data Serializer (TDS) is adapted for operation in pad or strip mode. It captures the Time-over-Threshold (ToT) pulses from the sTGC pads or the fast charge ADC data from the sTGC strips.
- The Slow Control Adapter (SCA) ASIC is used for the configuration of the ASICs and for environmental monitoring.

(a)

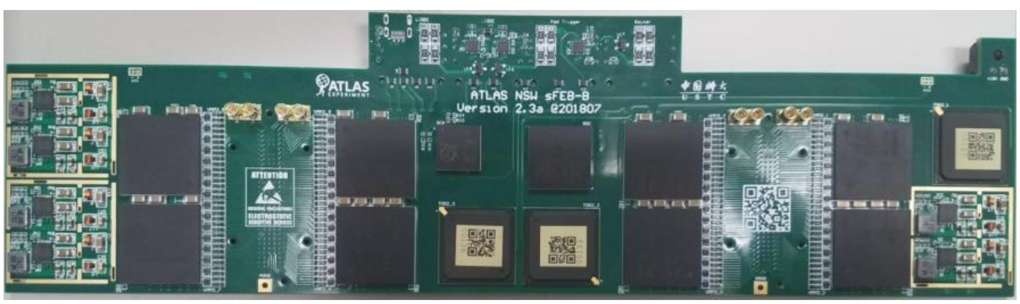

(b)

Figure 2.11: The sTGC front-end boards for (a) pads and (b) strips. [28]

The sTGC trigger chain is followed by the Pad Trigger Board and the Router Board, FPGA-based electronics cards that are installed near the rim of the NSW.

The Pad Trigger receives pad hits from the pad-TDS for all eight sTGC layers per sector and makes a trigger decision based on coincident hits in 3-out-of-4 layers in each quadruplet, independently. The PT coincidence logic, running in parallel with the strip data collection, sends trigger information back to the strip-TDS such as bunch crossing identification (BCID), strip-band ID and a second coordinate (ϕ) ID. This way it selects relevant charge data from the band of strips in each layer that passes through the tower generating the pad coincidence. The Router will collect the data packets from the active strip TDS and forward them to the sTGC Trigger Processor. The TP will compute centroids and track segments that point to the Big Wheel. The NSW muon candidates from the MM and the sTGC Trigger Processors are merged and subsequently sent to the Sector Logic to be combined with Big Wheel candidates. Finally, the Sector Logic sends the Level-1 trigger candidates to the ATLAS Muon Central Trigger Processor. The whole process repeats every bunch crossing with a fixed latency.

Chapter 3

ATLAS Local Trigger Interface (ALTI)

This chapter introduces the ATLAS Local Trigger Interface, a part of the experiment's Timing, Trigger and Control (TTC) system. ALTI is a custom made VME module, an upgrade to the current TTC modules, that will be deployed during the Long Shutdown II (LS2) at the LHC.

3.1 Introduction to the Level-1 trigger system and TTC system

The primary function of the LVL1 trigger system (Figure 3.1) is to form an initial trigger decision, based on reduced granularity information. This is achieved by looking for events with a potentially interesting physics signature at each bunch crossing. Input data/signals are received from a subset of detector systems, the calorimeter trigger system (L1Calo) and the muon trigger system (L1Muon), by identifying:

- high transverse-momentum (high-p_T) muons in the muon trigger system
- high-p_T electrons, photons, jets, and hadronically decaying taus in the electromagnetic and hadronic calorimeters.

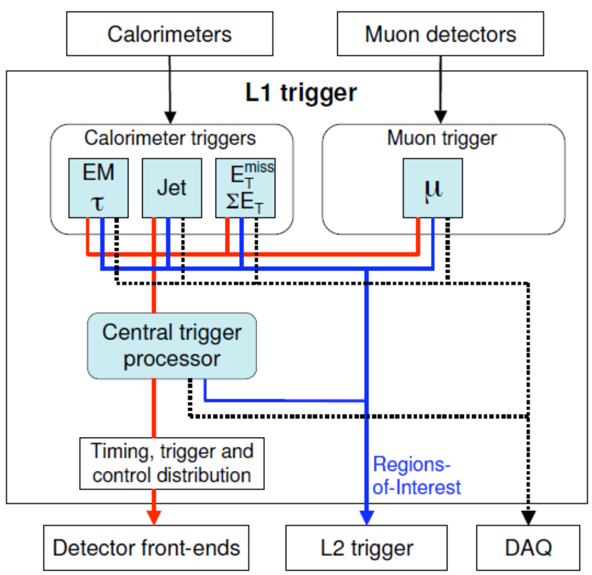

Figure 3.1: Block diagram of ATLAS Level-1 Trigger Level. [29]

The Level-1 Topological trigger system (L1Topo), a new addition to the LVL1 trigger system, combines this information and calculates variables used for LVL1 event selection such as topological quantities, geometric and kinematic relationships between L1Calo and L1Muon trigger objects (Figure 3.2).

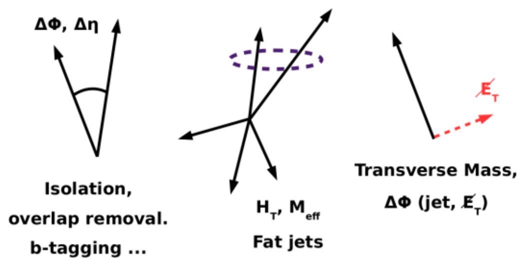

(a) (b) (c)

Figure 3.2: Examples of topologies used for topological trigger decisions by L1Topo (a) Angular separation (b) Hardness of the interaction (c) Invariant mass. [30]

Signals that are retained for further analysis are forwarded to the final subsystem, the Central Trigger Processor (CTP). The final trigger decision is made there, based on specific selection criteria (trigger menus), by combining and identifying interesting particle candidates coming from the previous trigger systems. Event rate is ultimately reduced to a maximum of 100 kHz. The corresponding event signal produced by the CTP is called the Level-1 trigger accept signal (L1A). Additionally, the CTP handles the deadtime of the experiment, preventing front-end data buffers from overflowing and aiding the readout process. Further details on the design of the LVL1 trigger system can be found in Ref. [15, 16, 17].

Following the LVL1 trigger system, the Timing, Trigger and Control (TTC) system is an optical broadcasting network which communicates with the front-end electronics and readout systems of the LHC detectors. The TTC system is responsible for distribution of synchronous timing and control signals within each detector electronic system by taking account of the appropriate phase relative to the LHC bunch structure and the different delays due to particle time-of-flight and signal propagation [31].

It provides the Level-1 trigger accept signal to the subdetectors, along with timing and synchronization signals such as the LHC 40 MHz clock (BC clock) and the Event Counter Reset (ECR). Table 3.1 summarizes the 22 digital TTC signals, both FORWARD (from the CTP to the detectors) and BACKWARD (from the detectors to the CTP) in direction.

The TTC system is composed of custom-made hardware electronics such as VME modules or boards and is partitioned in order to be able to run sub-detectors (or parts of sub-detectors) independently and in parallel. It utilizes a system developed in the RD12 collaboration, an optical-broadcast network connecting up to about 1024 destinations to each source. Triggers (channel A) and commands (channel B) are encoded and broadcast as a single optical signal, called the TTC stream, to all destinations (Figure 3.3).

TTC signal	Direction	Description
BC	forward	Bunch crossing clock: 40.079MHz, 50% duty ratio.
ORB	forward	Periodic signal representing one LHC turn. Period is 3564 bunch crossings; pulse width is 40 BC.
L1A	forward	Level-1 trigger accept signal of 1 BC pulse width.
TTR[3..1]	forward	Auxiliary triggers generated locally by the partition.
BGO[3..0]	forward	Signals for sending B-channel TTC commands.
TTYP[7..0]	forward	8-bit trigger type identification word associated with each L1A.
BUSY	backward	Used to inform the CTP to introduce L1A dead-time, i.e. throttle L1A generation when the readout buffers are overwhelmed.
CALREQ[2..0]	backward	3-bit word issued by the sub-detector and used by the CTP to generate calibration triggers.

Table 3.1: The TTC signals. [32]

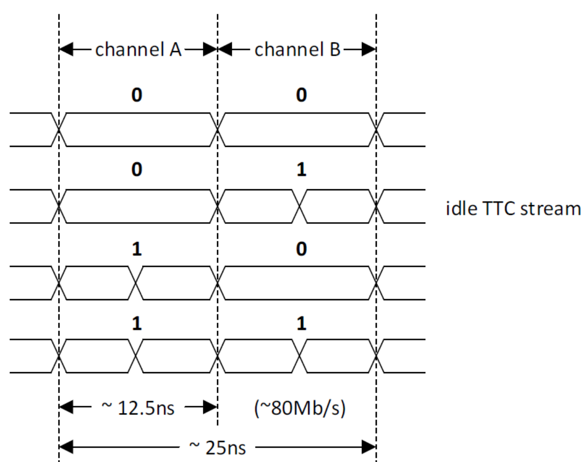

Figure 3.3: Time Division Multiplexing (TDM) of channels A and B and Bi-Phase Mark (BPM) encoding into the TTC stream. [32]

3.2 ALTI

An upgrade to the current TTC system at the ATLAS experiment will be the ATLAS Local Trigger Interface. ALTI is a new electronic board, designed to integrate the functionality of the four existing TTC modules and replace them with a single VME module (Figure 3.4).

The primary function of ALTI is to provide the interface between the CTP and the TTC optical broadcasting network, in order to distribute the TTC signals to the sub-detector electronics in the counting room or in the experimental cavern.

Figure 3.4: ALTI VME module. [33]

It receives TTC signals from the CTP through the Link-in cable and distributes them into the TTC system of the sub-detector through NIM outputs.

Motivation for the TTC upgrade is based on the difficulty to produce spares for the TTC modules or reproduce new ones. The current spare modules have obsolete and ageing components, along with limiting monitoring capabilities and firmware replacement issues. ALTI provides all existing functionalities, along with updated and new features, while preserving backward compatibility with the hardware of other modules.

3.2.1 Legacy TTC modules

The TTC modules that are currently being used in the ATLAS experiment are the Local Trigger Processor (LTP), the Local Trigger Processor Interface (LTPI), the TTC VMEbus Interface (TTCvi) and the TTC Encoder/Transmitter (TTCex) (Figure 3.5).

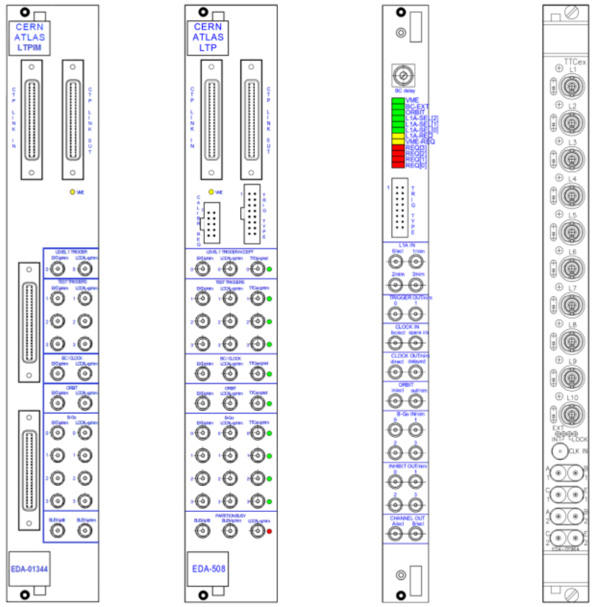

(a) (b) (c) (d)

Figure 3.5: Photo of Legacy TTC modules (front panel view): (a) LTPI, (b) LTP, (c) TTCvi, (d) TTCex. [32]

Each legacy module is described below:

- LTP: Receives timing and trigger signals from the CTP and propagates them to the TTC system through the TTCvi module.

- LTPi: Provides an interface between the CTP and LTP. It allows combined parallel running of TTC partitions between various subdetectors.

- TTCvi: Interfaces the local and the global TTC system (CTP). Generates the TTC signals for channel A and B based on the L1A signal, the ORBIT signal, external timing signals (BGO) and other data.

- TTCex: Receives electrical signals from TTCvi and performs the final encoding and the electrical-to-optical conversion.

3.2.2 Architecture and functionality of ALTI

ALTI is a custom-made 6U VME64x module that occupies two slots in a TTC VME crate. It is made out of two PCBs (Figure 3.6):

Motherboard
Houses all logic, implemented in discrete integrated circuits. It includes the Xilinx Artix-7 XCA200T FPGA, the power supply network, the Inter-Integrated Circuit (I2C) network, Random Access Memories (RAM), the VMEbus connectors, two Low-Voltage Differential Signaling (LVDS)-LINK input connectors, six Small Form-factor Pluggable (SFP) modules and the calibration request Registered Jack-45 (RJ45) connector.

Mezzanine card

The mezzanine is connected to the motherboard via a Samtec high-speed connector. It accommodates all of the coaxial input and output connectors as well as the two LVDS-LINK output connectors.

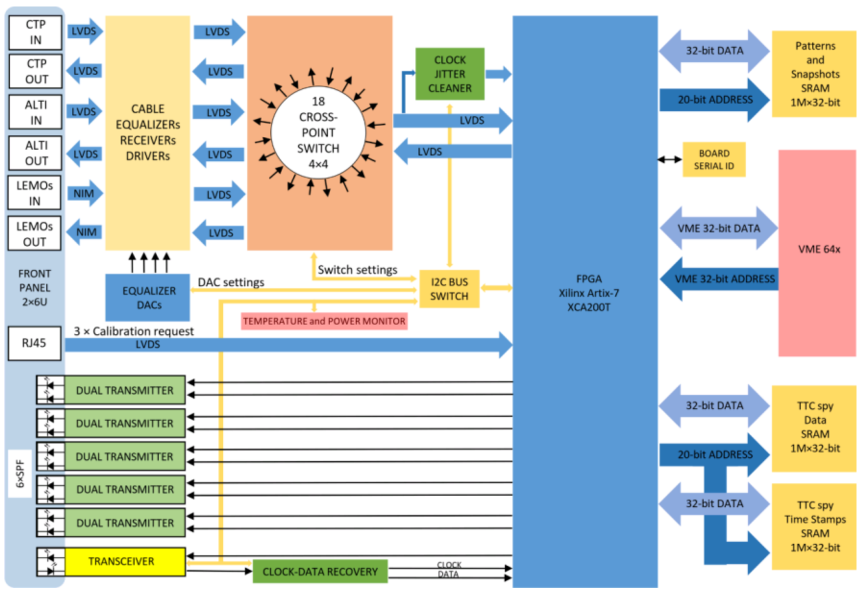

Figure 3.6: Functional block diagram of the ALTI hardware. [32]

Software has been developed in order to drive the ALTI module and integrate it into the run control system of the ATLAS experiment. It is divided into types of software:

Low-level software: Used for control, configuration and monitoring of the ALTI module. Executed on a single-board computer (SBC) of the ATLAS readout driver crate.

High-level software: Provides the run control application necessary to integrate the ALTI module into the ATLAS run control system and to allow its operation within the running experiment. It makes use of the low-level software for communication with the actual ALTI hardware.

ALTI preserves the functionalities of the legacy TTC modules, along with providing additional ones such as:

- Pattern generation
- Snapshot memory for the input signals
- Optical TTC stream analyser for decoding and monitoring of the output TTC stream.
- Input signal synchronization and coarse phase monitoring.
- Programmable phase shift: delay of the optical TTC output to adjust sub-detector BC timing.
- Improved monitoring capabilities e.g rate counters for TTC signals, per-BCID counters etc.
- Mini-CTP functionality (to be implemented) with a set of CTP-like functions: Lookup table (LUT) for trigger logic, simple and complex deadtime, pseudo-random triggers etc.

Chapter 4

ALTI TTC patterns

This chapter presents the ALTI pattern files which are used to program ALTI and convey the TTC information to the front-end electronics. The development of a software tool is described that allows the generation of configurable ALTI pattern files at various frequencies.

4.1 Pattern generation

In normal operation, ALTI receives the LHC clock and the TTC signals from the CTP and forwards them to the sub-detector electronics and readout systems through the optical TTC distribution network and FELIX. During LS2 no communication between the CTP and ALTI can be established. Therefore, ALTI utilizes a programmable pattern generator, that is accommodated in the FPGA, mainly for test and debugging purposes.

ALTI's pattern generator produces arbitrary numeric sequencies of bit patterns at the FPGA outputs. Each pattern is stored in an external 1Mx32-bit memory bank which contains a 21-bit wide pattern and a 11-bit wide multiplicity count (defines the duration of the pattern in BC) (Figure 4.1). These memory entries comprise the TTC signals, with each entry corresponding to 1 BC (24.9507 ns in duration).

31 … 21	20	19	18 … 16	15 … 8	7 … 4	3 … 1	0
BC_Multiplicity	ORB	BUSY	CALREQ2..0	TTYP7..0	BGO3..0	TTR3..1	L1A

Figure 4.1: ALTI pattern generation memory format. [32]

Pattern generation can be used in two modes, continuous (repeated in a loop) or in single-shot mode, with each TTC signal independently enabled and disabled from the pattern if needed. This functionality allows us configure ALTI's pattern generator with input pulse pattern files (Figure 4.2) of the following format:

- Vertical lines in the header represent the type of TTC pulse signal used in the pattern
- Parallel lines define the numeric bit that is assigned to that TTC signal

```
#----------------------
#                     M
#                     u
#                     l
#                     t
#                     i
#                     p
#                     l
#   CCC               i
#  BRRR    T BBBB TTT  c
#O UEEE    T GGGG TTTL i
#R SQQQ    Y OOOO RRR1 t
#B Y210    P 3210 321A y
#----------------------
 1 0000 0x00 0000 0000 40
 0 0000 0x00 0000 0000 100
 0 0000 0x00 0100 0000 1
 0 0000 0x00 0000 0000 100
 0 0000 0x81 0000 0001 1
 0 0000 0x81 0000 0000 4
 0 0000 0x00 0000 0000 100
 0 1000 0x00 0000 0000 200
 0 0000 0x00 0000 0000 3018
```

Figure 4.2: ALTI pattern input file containing TTC signals in one LHC orbit.

4.2 ALTI pulse pattern generator

A tool, using Python as a programming language and ROOT data analysis framework, was developed that provides the generation of ALTI pulse pattern files. The program integrates the TTC information in each generated pattern and allocates it in the required ALTI pattern format. It applies important parameters, electronic hardware restrictions, trigger rules and mechanisms on the generation of these patterns which are being used by the CTP in normal operation.

The motivation behind this tool is to produce pulse patterns that simulate realistic trigger conditions, program ALTI and study the response of the Trigger System for the New Small Wheel muon detector electronics. This procedure will facilitate developments related to the Trigger System validation and contribute to the verification of its operation and data readout process.

Pattern generation focuses on FORWARD type of TTC signals. The following TTC signals are used by the program:

- ORB: Timing signal indicating the beginning of a new LHC turn. The duration of the signal is 40 BC (1 us) and it is used as Bunch-Counter Reset (BCR) control command. This command resets the BC identifier and controls the phase of local bunch crossing counters at each LHC turn in order to maintain data synchronization.

- BGO2: B-Go commands used to trigger B-channel TTC commands. Currently used for test pulses.

- L1A: Level-1 accept pulse signal associated with a trigger (test pulse signal).

Three files are provided by the program: the ALTI pulse pattern file (type .dat), a file containing the generated data and information related to them (type .txt), and a file with histograms from the generated data (type .pdf).

4.2.1 Features and generated examples

Following are the notable features of this tool:

- Trigger Type

Two types of triggers are simulated: clocked test pulse signals, where the distance between consecutive triggers is fixed throughout the pattern file, and random test pulse signals, where the frequency of a trigger is random (Figure 4.3).

```
#                    M
#                    u
#                    l
#                    t
#                    i
#                    p
#                    l
#   CCC              i
#  BRRR    T BBBB TTT  c
#O UEEE    T GGGG TTTL i
#R SQQQ    Y OOOO RRR1 t
#B Y210    P 3210 321A y
#----------------------
 1 0000 0x00 0000 0000 40  # orbit signal
 0 0000 0x00 0000 0000 11
 0 0000 0x00 0000 0000 348
 0 0000 0x00 0100 0000 1
 0 0000 0x00 0000 0000 69
 0 0000 0x00 0000 0001 1
 0 0000 0x00 0000 0000 329
 0 0000 0x00 0100 0000 1
 0 0000 0x00 0000 0000 69
 0 0000 0x00 0000 0001 1
 0 0000 0x00 0000 0000 329
 0 0000 0x00 0100 0000 1
 0 0000 0x00 0000 0000 69
 0 0000 0x00 0000 0001 1
 0 0000 0x00 0000 0000 329
 0 0000 0x00 0100 0000 1
 0 0000 0x00 0000 0000 69
 0 0000 0x00 0000 0001 1
 0 0000 0x00 0000 0000 329
 0 0000 0x00 0100 0000 1
 0 0000 0x00 0000 0000 69
 0 0000 0x00 0000 0001 1
 0 0000 0x00 0000 0000 329
 0 0000 0x00 0100 0000 1
 0 0000 0x00 0000 0000 69
 0 0000 0x00 0000 0001 1
 0 0000 0x00 0000 0000 329
 0 0000 0x00 0100 0000 1
 0 0000 0x00 0000 0000 69
 0 0000 0x00 0000 0001 1
 0 0000 0x00 0000 0000 329
 0 0000 0x00 0100 0000 1
 0 0000 0x00 0000 0000 69
 0 0000 0x00 0000 0001 1
 0 0000 0x00 0000 0000 294
 .
 .
```

(a)

```
#                    M
#                    u
#                    l
#                    t
#                    i
#                    p
#                    l
#   CCC              i
#  BRRR    T BBBB TTT  c
#O UEEE    T GGGG TTTL i
#R SQQQ    Y OOOO RRR1 t
#B Y210    P 3210 321A y
#----------------------
 1 0000 0x00 0000 0000 40  # orbit signal
 0 0000 0x00 0000 0000 11
 0 0000 0x00 0000 0000 415
 0 0000 0x00 0100 0000 1
 0 0000 0x00 0000 0000 69
 0 0000 0x00 0000 0001 1
 0 0000 0x00 0000 0000 99
 0 0000 0x00 0100 0000 1
 0 0000 0x00 0000 0000 69
 0 0000 0x00 0000 0001 1
 0 0000 0x00 0000 0000 148
 0 0000 0x00 0100 0000 1
 0 0000 0x00 0000 0000 69
 0 0000 0x00 0000 0001 1
 0 0000 0x00 0000 0000 958
 0 0000 0x00 0100 0000 1
 0 0000 0x00 0000 0000 69
 0 0000 0x00 0000 0001 1
 0 0000 0x00 0000 0000 447
 0 0000 0x00 0100 0000 1
 0 0000 0x00 0000 0000 69
 0 0000 0x00 0000 0001 1
 0 0000 0x00 0000 0000 123
 0 0000 0x00 0100 0000 1
 0 0000 0x00 0000 0000 69
 0 0000 0x00 0000 0001 1
 0 0000 0x00 0000 0000 157
 0 0000 0x00 0100 0000 1
 0 0000 0x00 0000 0000 69
 0 0000 0x00 0000 0001 1
 0 0000 0x00 0000 0000 271
 0 0000 0x00 0100 0000 1
 0 0000 0x00 0000 0000 69
 0 0000 0x00 0000 0001 1
 0 0000 0x00 0000 0000 84
 0 0000 0x00 0100 0000 1
 0 0000 0x00 0000 0000 69
 0 0000 0x00 0000 0001 1
 0 0000 0x00 0000 0000 172
 .
 .
```

(b)

Figure 4.3: Pulse pattern generated at 100 kHz, 70 BC test pulse - L1A latency (a) Clocked trigger type (b) Random trigger type.

Each event is assigned with a BCID that defines the bunch crossing at which the event occurred within an LHC turn. Potential bunch crossings are numbered 0 to 3563 per LHC orbit.

For random trigger type, a pdf of histograms is provided that stores BCIDs of generated test pulse and L1A signals. Additional histogram depicts the probability of a bunch crossing to occur, which follows a Poisson distribution (Figure 4.4). It decreases exponentially over time while the mean rate is inversely proportional to the frequency of a bunch crossing in each LHC orbit.

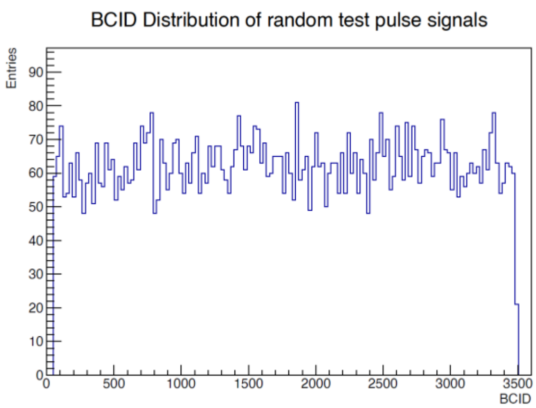

(a)

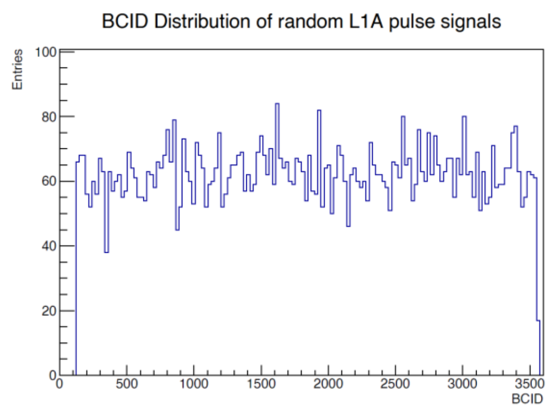

(b)

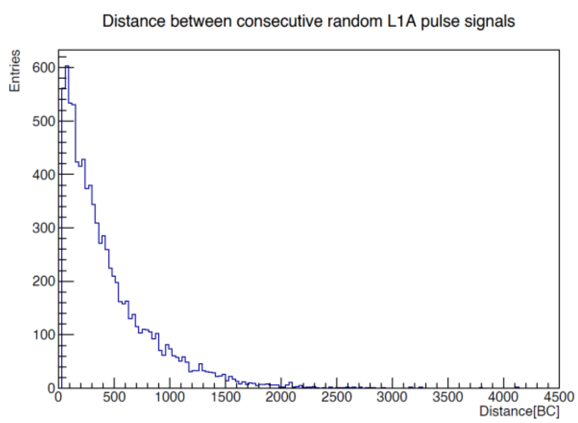

(c)

Figure 4.4: Histograms for random trigger type generated at 100 kHz, 70 BC test pulse – L1A signal latency. (a) BCID Distribution of random test pulse signals. (b) BCID Distribution of random L1A pulse signals. (c) Distance between consecutive L1A pulse signals (in BC).

- Latency

Latency is a configurable parameter and it is defined as the separation (in BC) between the arrival of a test pulse signal in an LHC orbit and the L1A signal that corresponds to it (Figure 4.5).

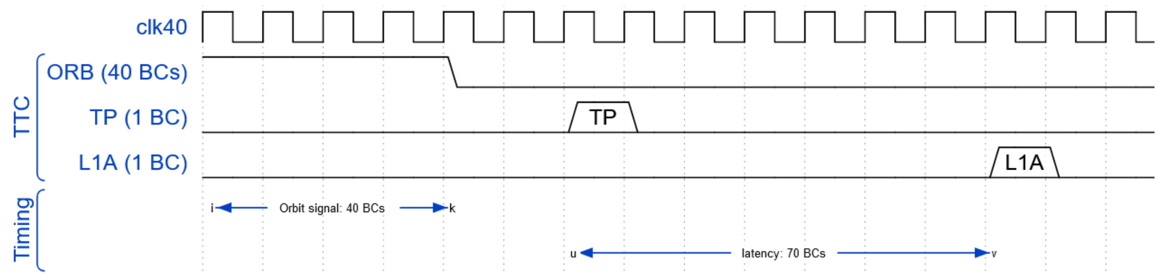

Figure 4.5: Time diagram for a clocked pulse pattern generated at 100 kHz, 70 BC test pulse - L1A latency (clock out of scale).

- Content

Apart from the ORB signal, the type of the remaining TTC signals on each LHC orbit can be customized. The generated pattern file may contain only test pulse signals, only L1A signals or both types of signals (Figure 4.6).

```
#-----------------------
#                      M
#                      u
#                      l
#                      t
#                      i
#                      p
#                      l
#   CCC                i
#  BRRR    T BBBB TTT  c
#O UEEE    T GGGG TTTL i
#R SQQQ    Y OOOO RRR1 t
#B Y210    P 3210 321A y
#-----------------------
 1 0000 0x00 0000 0000 40  # orbit signal
 0 0000 0x00 0000 0000 11
 0 0000 0x00 0000 0000 348
 0 0000 0x00 0100 0000 1   # test pulse signal
 0 0000 0x00 0000 0000 399
 0 0000 0x00 0100 0000 1
 0 0000 0x00 0000 0000 399
 0 0000 0x00 0100 0000 1
 0 0000 0x00 0000 0000 399
 0 0000 0x00 0100 0000 1
 0 0000 0x00 0000 0000 399
 0 0000 0x00 0100 0000 1
 0 0000 0x00 0000 0000 399
 0 0000 0x00 0100 0000 1
 0 0000 0x00 0000 0000 399
 0 0000 0x00 0100 0000 1
 0 0000 0x00 0000 0000 399
 0 0000 0x00 0100 0000 1
 0 0000 0x00 0000 0000 364
 .
 .
```

(a)

```
#-----------------------
#                      M
#                      u
#                      l
#                      t
#                      i
#                      p
#                      l
#   CCC                i
#  BRRR    T BBBB TTT  c
#O UEEE    T GGGG TTTL i
#R SQQQ    Y OOOO RRR1 t
#B Y210    P 3210 321A y
#-----------------------
 1 0000 0x00 0000 0000 40 # orbit signal
 0 0000 0x00 0000 0000 11
 0 0000 0x00 0000 0000 418
 0 0000 0x00 0000 0001 1  # L1A signal
 0 0000 0x00 0000 0000 399
 0 0000 0x00 0000 0001 1
 0 0000 0x00 0000 0000 399
 0 0000 0x00 0000 0001 1
 0 0000 0x00 0000 0000 399
 0 0000 0x00 0000 0001 1
 0 0000 0x00 0000 0000 399
 0 0000 0x00 0000 0001 1
 0 0000 0x00 0000 0000 399
 0 0000 0x00 0000 0001 1
 0 0000 0x00 0000 0000 399
 0 0000 0x00 0000 0001 1
 0 0000 0x00 0000 0000 399
 0 0000 0x00 0000 0001 1
 0 0000 0x00 0000 0000 294
 .
 .
```

(b)

Figure 4.6: Clocked pulse pattern generated at 100 kHz, 70 BC test pulse - L1A latency (a) Containing only test pulse signals (b) Containing only L1A signals.

- LHC beam structure

The LHC beam structure can be applied on the generated data for random trigger type. A depiction of the structure is available on the produced histograms (.pdf file).

In the following histograms, the BCIDs of generated test pulse and L1A signals are evenly distributed along an LHC orbit and in agreement with the LHC bream structure (Figure 4.7).

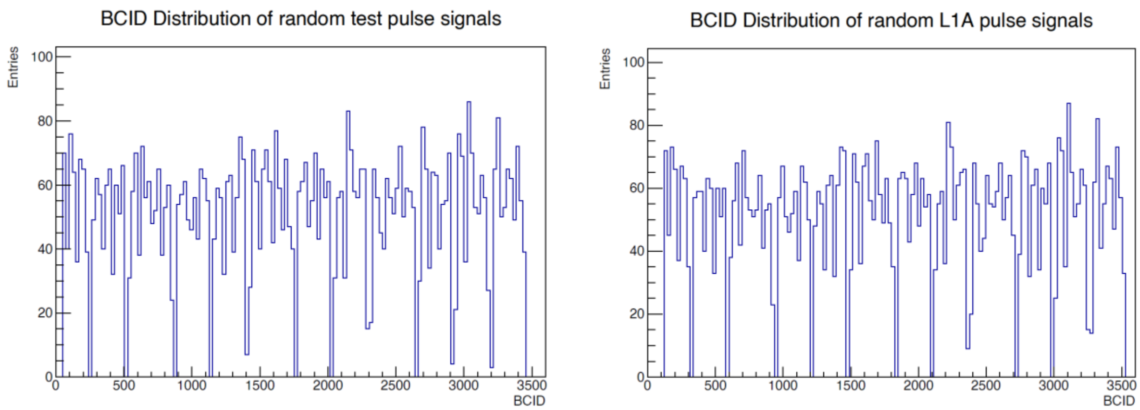

(a) (b)

Figure 4.7: LHC beam structure applied on BCID distributions for random trigger type. Generated at 100 kHz, 70 BC test pulse – L1A signal latency. (a) BCID Distribution of random test pulse signals. (b) BCID Distribution of random L1A pulse signals.

- Trigger rules – mechanisms

CTP employs trigger rules in order to control the L1A trigger rate and minimize BUSY signals from sub-systems of the ATLAS detectors. To achieve that, the following mechanisms are implemented:

- Simple deadtime
  Preventive deadtime is introduced by the CTP: a programmable number of BC (currently at 4 BC) following the arrival of an L1A signal during which other L1A signals are vetoed. It is used to prevent overlapping of readout time-frames for some front-end systems.

- Complex deadtime - “Leaky” bucket algorithm
  The algorithm is used to prevent front-end buffers from filling up. It is defined by the size S of the front-end electronic buffers (depicted as a bucket in Figure 4.8) and the trigger transmit rate R. The values of the parameters S and R directly determine the values of the parameters defining the deadtime, i.e. the time period and the maximum number of L1A signals issued during this time period.

  At the arrival of each L1A signal the bucket’s counter is incremented by +1 and, every R BCIDs, decreases by -1. Deadtime is introduced when the counter is equal to the size of the bucket, when buffers are full.

The following buckets (ratio S / R) were used in Run 2:

- o bucket 0: 15 / 370 for L1Calo and CSC
- o bucket 1: 42 / 384 for TRT
- o bucket 2: 9 / 351 for LAr
- o bucket 3: 14 / 260 for L1Topo (fully in the shadow of bucket 2)

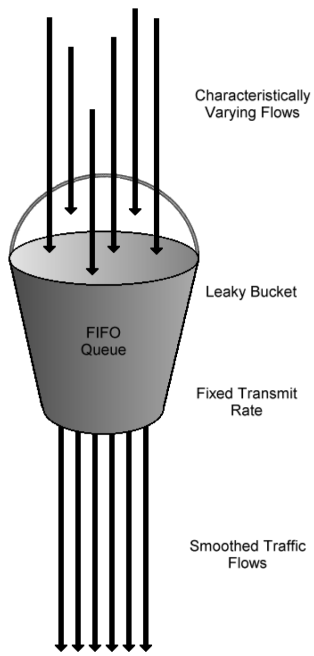

Figure 4.8: “Leaky” bucket algorithm. [34]

- Sliding window: Maximum 15 L1A signals in 3600 BC
  Prevents front-end electronics of the ATLAS Pixel detector (part of Inner Detector) to suffer from data de-synchronization due to single very large background event.

The program incorporates the aforementioned trigger mechanisms along with additional trigger rules related to orbit duration, input frequency limits, hardware/software limitations etc.

Chapter 5

ALTI pattern tests

This chapter summarizes a series of tests that have been carried out at the Vertical Slice Lab - CERN in order to validate the pattern tool's results.

5.1 Introduction to the readout procedure

In order to verify the tool's functionality, ALTI was configured with pulse pattern files generated at different rates, both for clocked and random trigger type. The following schematics depicts the NSW TDAQ electronic dataflow, with the red squares indicating the regions of interest (Figure 5.1). The sTGC NSW trigger electronics (upper part), that is the front-end boards and the Pad Trigger, were configured and bi-directional communication with GBT-SCA e-links on said boards was established. This is achieved through the FELIX system and OPC UA Server [35]. In detail, test sequence is as follows:

- ALTI (TTC in the schematics) is configured with a generated pulse pattern and forwards the TTC information through FELIX and the optical TTC network to the sTGC FEBs.
- TTC information is distributed to the electronics via the ROC.
- At the VMM ASIC of the pad FEBs, ALTI's test pulse signal is received. VMMs generate a test pulse at the next BC.
- The signal is processed by the Trigger Data Serializer (pad TDS on the FEBs), where the appropriate selection algorithm is applied, and subsequently is sent to the PT.

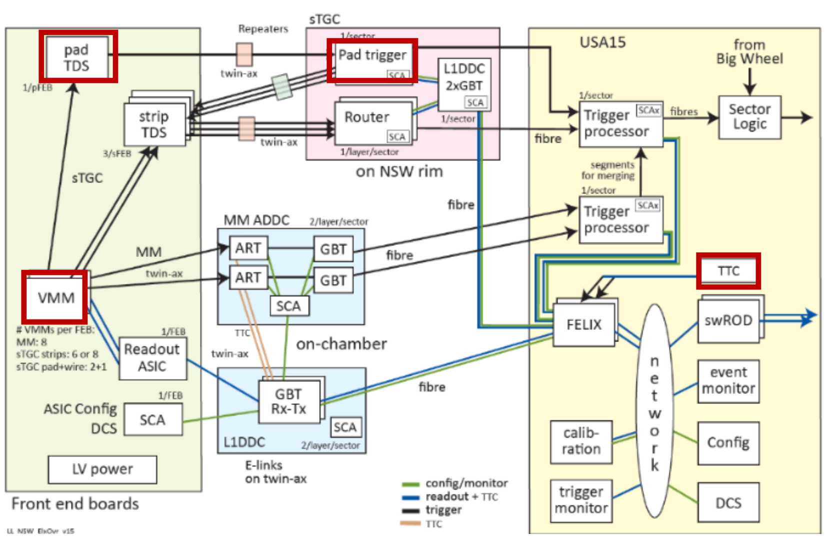

Figure 5.1 Schematic of NSW trigger and DAQ electronics. For the PT readout tests, data transmission happens via the rim L1DDC.

NetIO publish/subscribe system was used to obtain distributed data from the Pad Trigger. The system connects with FELIX via felixcore, an application that is the central process of a FELIX system, allowing the user to interact with it via network endpoints and receive/send data from/to E-links.

Data analysis, using software development in C++ and ROOT framework, aims to study the response of the FEBs/Pad Trigger under these conditions. Additionally, it focuses on validating that the TTC signals are processed and transmitted successfully by/to the individual electronics.

5.2 Tests with the sTGC Pad Trigger

5.2.1 Readout data format

Each netio_cat data packet obtained from the sTGC Pad Trigger has a raw encoding. Pad Trigger's readout data format (Figure 5.2(a)) was used, along with software development, to decode and analyze the data.

<table>
<tr><th>Bit number</th><th>15</th><th>14</th><th>13</th><th>12</th><th>11</th><th>10</th><th>9</th><th>8</th><th>7</th><th>6</th><th>5</th><th>4</th><th>3</th><th>2</th><th>1</th><th>0</th></tr>
<tr><td>E-link start of packet</td><td colspan="8">K28.5 ("BC")</td><td colspan="8">K28.1 ("3C")</td></tr>
<tr><td rowspan="4">NSW standard readout header</td><td colspan="4">fragID</td><td colspan="4">secID</td><td>EC</td><td colspan="7">FLAGS</td></tr>
<tr><td colspan="12">BCID (when L1A arrived)</td><td colspan="2">ORBIT</td><td colspan="2">SPARE</td></tr>
<tr><td colspan="16">L1ID(31:16)</td></tr>
<tr><td colspan="16">L1ID(15:0)</td></tr>
<tr><td rowspan="12">Pad readout packet (repeated 24 times)</td><td colspan="4">A</td><td colspan="7">0</td><td colspan="5">pFEB address (0 to 23)</td></tr>
<tr><td colspan="4">B</td><td colspan="12">Pad BCID (when pFEB Pad hit pattern arrived)</td></tr>
<tr><td colspan="4">C</td><td colspan="12">pFEB BCID</td></tr>
<tr><td colspan="4">9</td><td colspan="4">0</td><td colspan="8">pFEB Pad hits (103:96)</td></tr>
<tr><td colspan="4">8</td><td colspan="12">pFEB Pad hits (95:84)</td></tr>
<tr><td colspan="4">7</td><td colspan="12">pFEB Pad hits (83:72)</td></tr>
<tr><td colspan="4">6</td><td colspan="12">pFEB Pad hits (71:60)</td></tr>
<tr><td colspan="4">5</td><td colspan="12">pFEB Pad hits (59:48)</td></tr>
<tr><td colspan="4">4</td><td colspan="12">pFEB Pad hits (47:36)</td></tr>
<tr><td colspan="4">3</td><td colspan="12">pFEB Pad hits (35:24)</td></tr>
<tr><td colspan="4">2</td><td colspan="12">pFEB Pad hits (23:12)</td></tr>
<tr><td colspan="4">1</td><td colspan="12">pFEB Pad hits (11:0)</td></tr>
<tr><td>E-link end of packet</td><td colspan="8">K28.6 ("DC")</td><td colspan="8">K28.5 ("BC")</td></tr>
</table>

(a)

```
>>> message from 128.141.214.253:36404, size=1744
d0 06 00 00 e1 02 00 00 00 00 6b 70 00 00 00 03
a0 00 b6 9a c6 97 90 ff 8f ff 7f ff 6f ff 5f ff 4f ff 3f ff 2f ff 1f ff
a0 01 b6 9a c6 97 90 ff 8f ff 7f ff 6f ff 5f ff 4f ff 3f ff 2f ff 1f ff
a0 02 b6 9a c6 97 90 ff 8f ff 7f ff 6f ff 5f ff 4f ff 3f ff 2f ff 1f ff
a0 03 b6 9a c6 97 90 ff 8f ff 7f ff 6f ff 5f ff 4f ff 3f ff 2f ff 1f ff
a0 04 b6 9a c5 55 90 55 85 55 75 55 65 55 55 55 45 55 35 55 25 55 15 55
a0 05 b6 9a c5 55 90 55 85 55 75 55 65 55 55 55 45 55 35 55 25 55 15 55
a0 06 b6 9a c5 55 90 55 85 55 75 55 65 55 55 55 45 55 35 55 25 55 15 55
a0 07 b6 9a c5 55 90 55 85 55 75 55 65 55 55 55 45 55 35 55 25 55 15 55
a0 08 b6 9a c5 55 90 55 85 55 75 55 65 55 55 55 45 55 35 55 25 55 15 55
a0 09 b6 9a c5 55 90 55 85 55 75 55 65 55 55 55 45 55 35 55 25 55 15 55
a0 0a b6 9a c5 55 90 55 85 55 75 55 65 55 55 55 45 55 35 55 25 55 15 55
a0 0b b6 9a c5 55 90 55 85 55 75 55 65 55 55 55 45 55 35 55 25 55 15 55
a0 0c b6 9a c6 97 90 ff 8f ff 7f ff 6f ff 5f ff 4f ff 3f ff 2f ff 1f ff
a0 0d b6 9a c6 97 90 ff 8f ff 7e ff 6f ff 5f ff 4f ff 3f ff 2f ff 1f ff
a0 0e b6 9a c6 97 90 ff 8f ff 7f ff 6f ff 5f ff 4f ff 3f ff 2f ff 1f ff
a0 0f b6 9a c6 97 90 ff 8f ff 7f ff 6f ff 5f ff 4f ff 3f ff 2f ff 1f ff
a0 10 b6 9a c5 55 90 55 85 55 75 55 65 55 55 55 45 55 35 55 25 55 15 55
a0 11 b6 9a c5 55 90 55 85 55 75 55 65 55 55 55 45 55 35 55 25 55 15 55
a0 12 b6 9a c5 55 90 55 85 55 75 55 65 55 55 55 45 55 35 55 25 55 15 55
a0 13 b6 9a c5 55 90 55 85 55 75 55 65 55 55 55 45 55 35 55 25 55 15 55
a0 14 b6 9a c6 97 90 ff 8f ff 7f ff 6f ff 5f ff 4f ff 3f ff 2f ff 1f ff
a0 15 b6 9a c6 97 90 ff 8f ff 7f ff 6f ff 5f ff 4f ff 3f ff 2f ff 1f ff
a0 16 b6 9a c6 97 90 ff 8f ff 7f ff 6f ff 5f ff 4f ff 3f ff 2f ff 1f ff
a0 17 b6 9a c6 97 90 ff 8f ff 7f ff 6f ff 5f ff 4f ff 3f ff 2f ff 1f ff
```

(b)

Figure 5.2: (a) Pad Trigger readout data format (b) Netio_cat data packet obtained at 10kHz for clocked trigger type (first data readout window). [36]

A netio_cat message (Figure 5.2(b)) contains a pad readout data packet that is repeated 24 times (once per pFEB in one sTGC sector) per data readout window (up to three BC). Currently, PT receives data from 12 pFEBs since VS setup hosts half a sector. It stores information on pFEB address, pFEB BCIDs assigned to the generated test pulse signals, pad BCIDs when pFEB data arrived on PT, pad number that received hits etc.

5.2.2 Analysis

ALTI pulse patterns generated at frequencies between 0.001 Hz and 15 kHz, for both trigger types, were used. The sTGC pFEBs produced a test pulse signal according to the trigger type that was used (Figure 5.3).

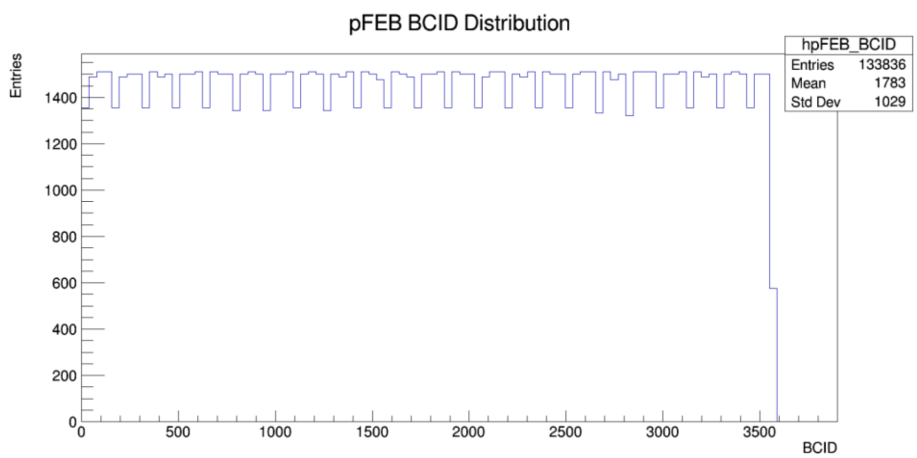

(a)

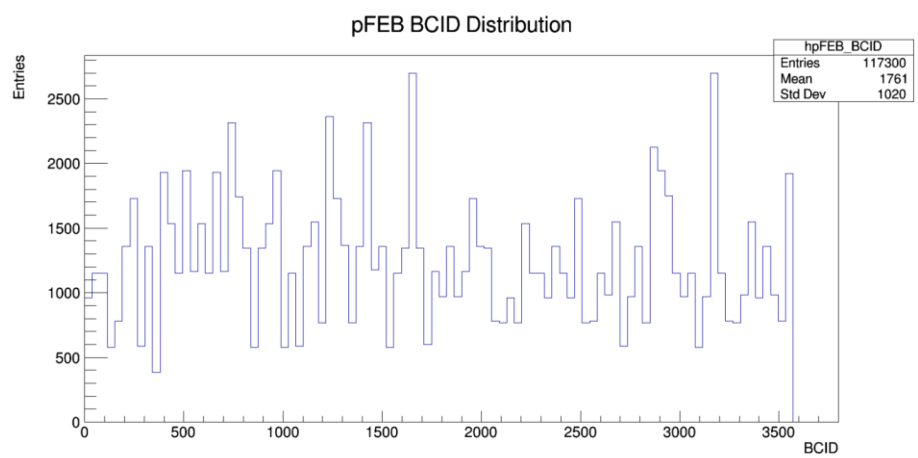

(b)

Figure 5.3: pFEB BCID distribution for pulse patterns generated at 1kHz (a) Clocked test pulse signals. (b) Random test pulse signals.

Similar BCID distribution was observed for the pad BCIDs, the BCIDs that the PT assigns to arriving pFEB pad hits (Figure 5.4). The fluctuations in the BCID distribution of random test pulse signals can be explained from ALTI's pattern generator operation mode: when used in continuous mode, the BCID assignment is initially random but after a few repetitions of the same ALTI pattern file the same BCIDs will eventually be reassigned.

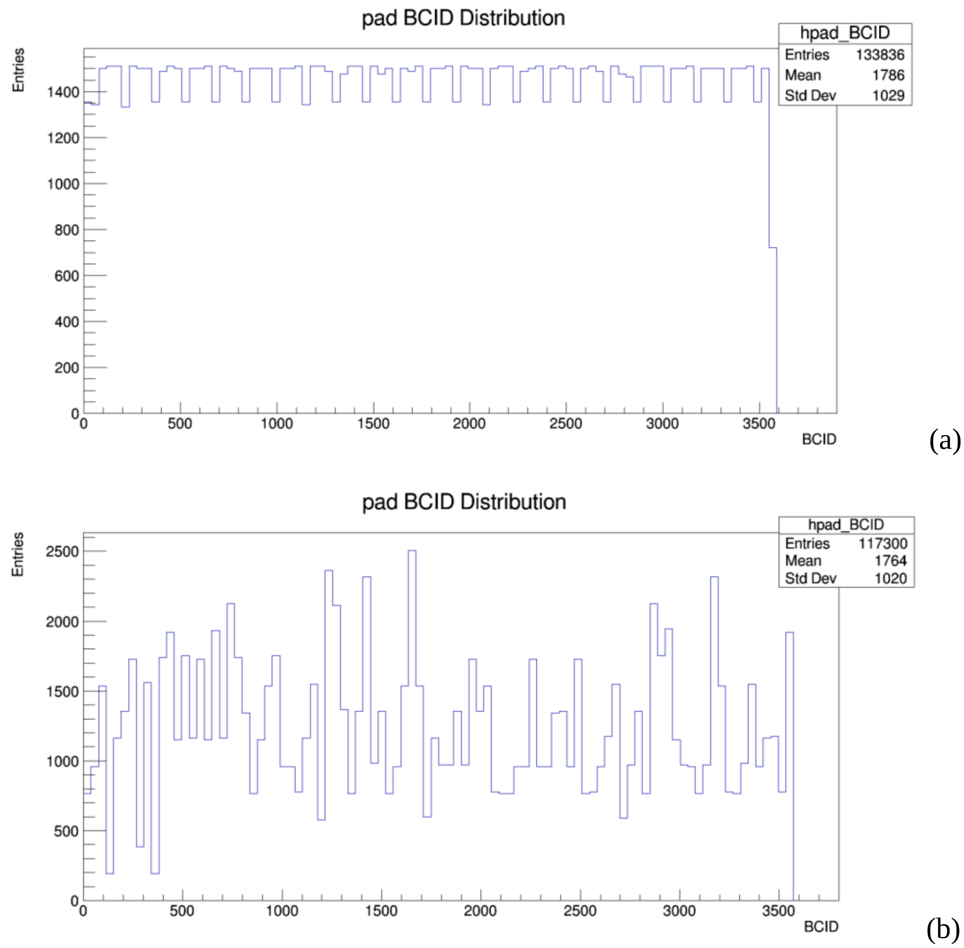

Figure 5.4: Pad BCID distribution for pulse patterns generated at 1kHz (a) Clocked test pulse signals. (b) Random test pulse signals.

Data analysis focused on observing the behavior of the sTGC trigger electronics in the readout path. One way to validate that the TTC signals are processed and transmitted successfully by/to the individual electronics is to measure the timing difference in signal transmission between them using BCID. In detail:

- Timing difference between test pulse BCIDs in the ALTI pattern file and the pFEBs BCIDs, as assigned to generated test pulses, was observed at 1 BC for clocked operation (Figure 5.5(a)). This is expected in both trigger types, but for random triggers the timing difference is not always stable.

- Timing difference between the pFEB BCIDs and the pad BCIDs is at 3 BC, both for clocked and random operation (Figure 5.5(b)). This is in agreement with the firmware that was used to program the PT's FPGA board which defines the BCID assignment.

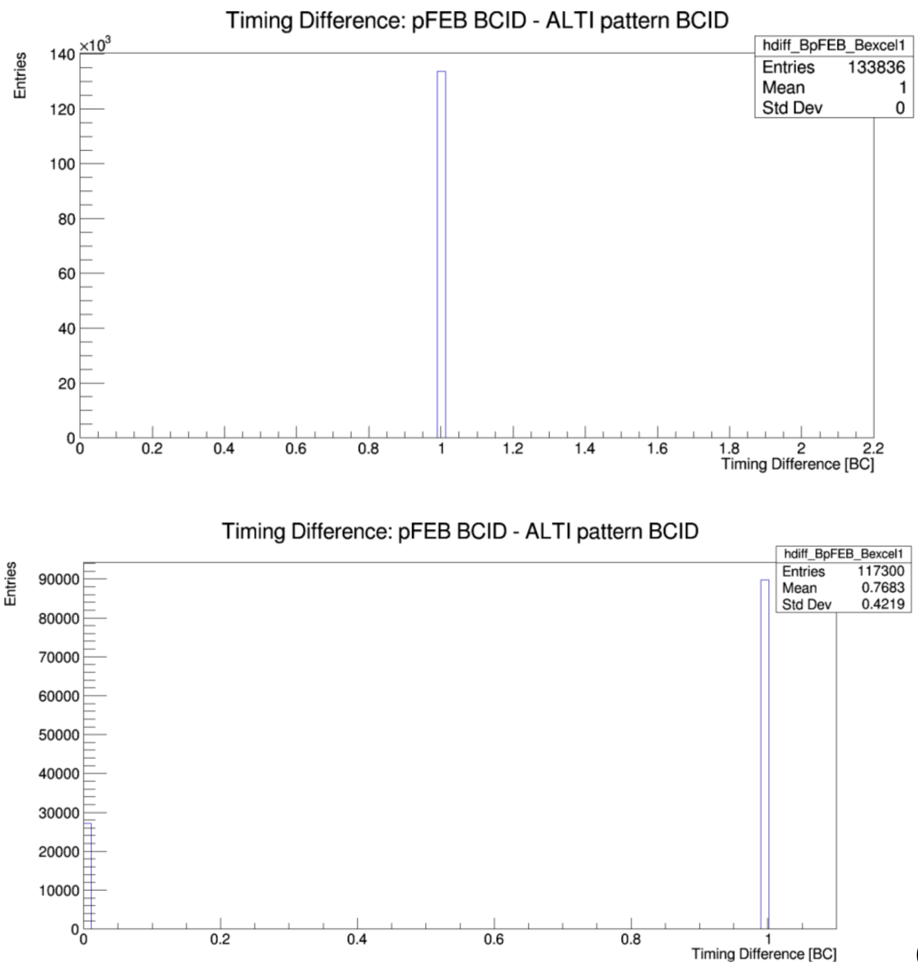

(a)

(b)

Figure 5.5: Timing differences (pFEB BCID – ALTI BCID) for pulse patterns generated at 10 kHz. (a) Clocked test pulse signals. (b) Random test pulse signals.

For the random operation, we observed that the correct assignment of the test pulse BCID is not always successful. The timing difference varies from zero to negative values and sometimes there is no BCID correlation at all with the test pulse BCIDs that were sent through the ALTI pattern file. This is a behavior that is under investigation.

The TTC transmission from the pad FEBs to the PT reported no errors, both for clocked and random operation (Figure 5.6).

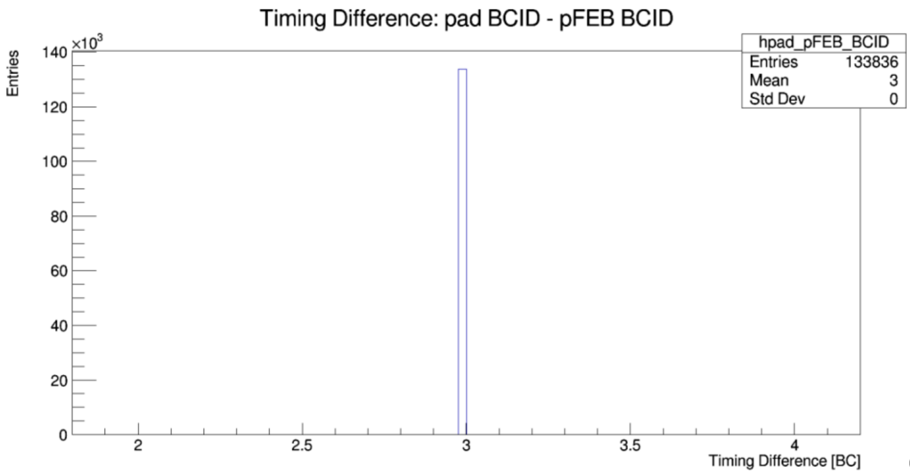

(a)

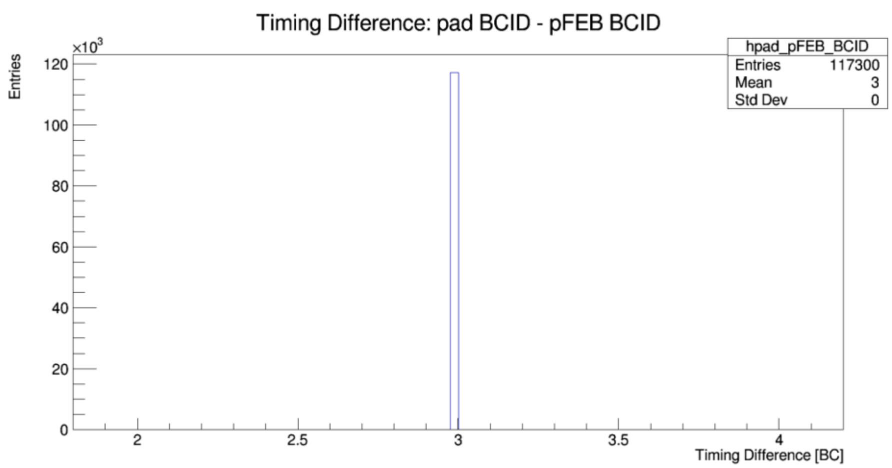

(b)

Figure 5.6: Timing differences (pad BCID - pFEB BCID) for pulse patterns generated at 10 kHz. (a) Clocked test pulse signals. (b) Random test pulse signals.

Chapter 6

Muon test beam analysis with NSW sTGC detectors

This chapter describes the muon test beam analysis with sTGC detectors at the Gamma Irradiation Facility (GIF^{++}) – CERN. An sTGC Quadruplet was placed close to a ^{137}Cesium radiation source, between 4 scintillators, while the H4 muon beam line was activated. One of the key objectives was the study of the sTGC pad efficiency by observing pad coincidences in the sTGC quadruplet.

6.1 Introduction to GIF^{++}

The Gamma Irradiation Facility (GIF) at CERN was located at the CERN SPS West Area and was extensively used from 1997 until its closure in 2014 for the characterization of LHC particle detectors. In order to cope with the HL-LHC requirements, a new GIF facility (GIF^{++}) was designed and built during the LS1 period, as a successor to the GIF. It is located at the North Area of the SPS in the EHN1 H4 beam line and has been fully operational since 2015 [37].

GIF^{++} (Figure 6.1) combines high-energy particle beams (mainly muon beams) together with gamma irradiations by a 14 TBq ^{137}Cesium source (as of 2014). The gamma fields (≤ 2.2 Gy/h) are used mainly for ageing studies or to simulate expected background conditions, whereas the muon beam is used to investigate the detectors' tracking performance under these conditions. In detail:

- The irradiator offers two adjustable gamma irradiation zones: upstream and downstream the irradiator with respect to the beam line direction. This is achieved using two panoramic collimators with angular correction filters and independent attenuation filter systems at both sides. (Figure 6.2(a)). The source activity provides a uniform photon flux of $E_\gamma = 662\ keV$ photons and accumulates doses equivalent to HL-LHC experimental conditions (Figure 6.2(b)).

- The muon beam is generated as a secondary beam, from the primary SPS proton beam on a production target. The spill structure follows the primary beam structure, which has a spill of 4.8 s with a close to flat distribution. It delivers a maximum muon flux of 10^4 particles per spill every ~30 s, with muon momentum in the range of $p_{muon} = 10 - 400\ GeV/c$.

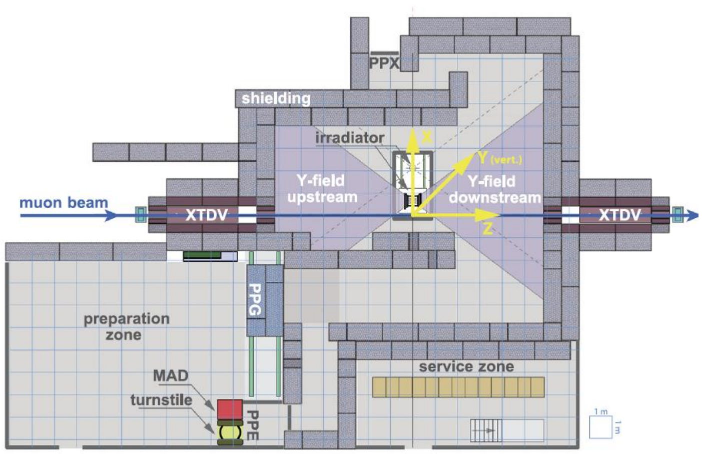

Figure 6.1: Layout of the new GIF^{++} facility. The position of the muon beam, the irradiator and the surface of the two irradiation areas are indicated. [37]

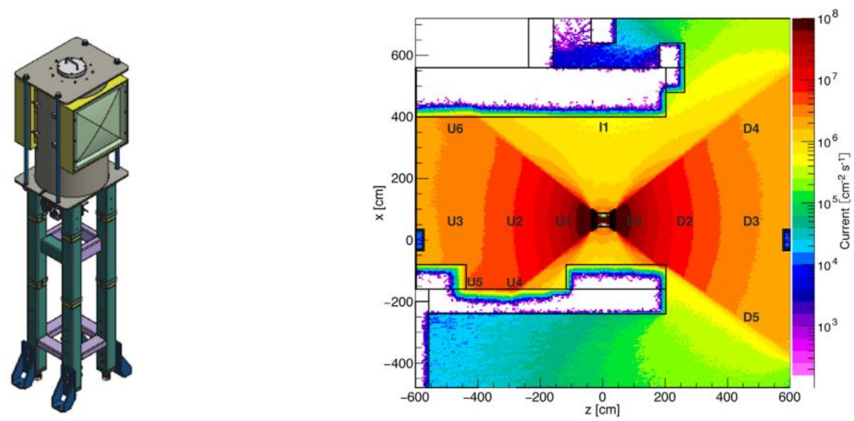

(a) (b)

Figure 6.2: (a) Schematic of the GIF^{++} irradiator with angular correction filters and independent filter systems at both sides. The two collimators have vertically and horizontally an opening of ±37° with respect to the beam axis. (b) Simulation of the total current of $E_{\gamma} = 662\ keV$ photons in the x-z plane (unattenuated). [37]

Located upstream of the GIF^{++} facility, a dedicated "Pre-Dump" was installed to allow an alternative production of muons from a high intensity pion beam directly in front of the irradiation bunker. According to Monte Carlo simulations of the H4 beam line, a better focused and more efficient muon beam is expected [38].

GIF^{++} was motivated by the new challenges for particle detector technologies that the HL-LHC upgrade is setting. The increase in luminosity will produce a background in the gas-based muon detectors that is ten times higher than the present one. Therefore, extensive studies on the operation and stability of particle detectors under such conditions are crucial. GIF^{++} allows us to gain detailed knowledge of the detector performance in the presence of high particle fluxes and insight to the possible ageing effects of the detector materials under continuous particle interactions.

6.2 Setup and preparation

During test beam period (Oct-Nov 2021), one sTGC quadruplet (QL1C4) was setup at GIF++ in combination with MicroMegas mechanical frame (Figure 6.3). It constitutes one large quad that includes 4 active layers of sTGC detector technology. The sTGC frame was installed on tilting part of MMs frame, at a 3 m distance from the radiation source.

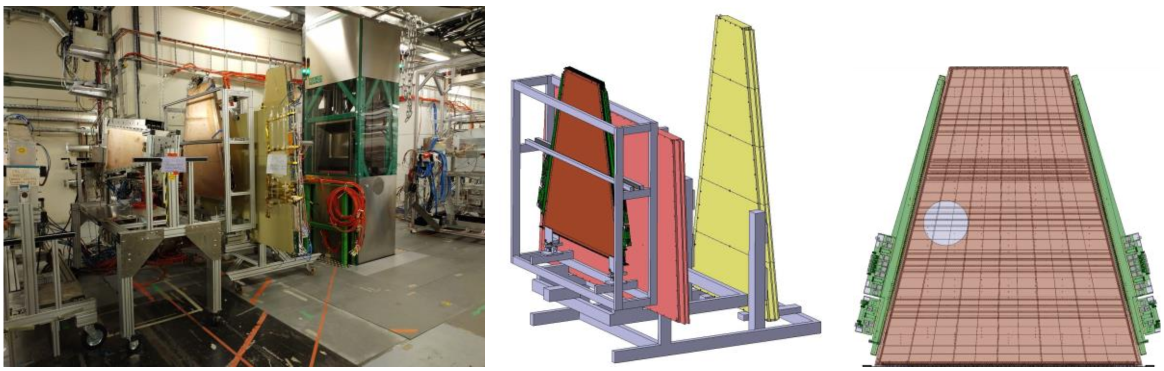

(a) (b) (c)

Figure 6.3: (a) sTGC quadruplet used at GIF++ during test beam period. (b) Placed on MM frame. (c) Rough estimation of test beam position on QL1C4. [39]

The following GIF++ services and running conditions were used for the sTGC data measurements (emphasis on pad efficiency studies):

- Beam radius: 10 cm
- Gas mixture: CO_2 (55%) : C_5H_{12} (45%)
- High Voltage: 2800 V
- Scintillator coincidences used: sTGC scintillator + GIF scintillator coincidence
- Readout: QL1C4 is equipped with front-end boards: pFEBs and sFEBs, FELIX, swROD, ALTI, L1DDC and an oscilloscope were used for data readout and tuning the scintillator coincidence.
- Radiation source conditions:
  - γ background
  - Rate: 13 $kHz\ /\ cm^2$
  - Multiple attenuation filters: 1, 1.5, 2.2, 3.3, 4.6, 6.9, 10, 15, 22, 46 ,69, 100
- Angle (with respect to the test beam direction): 0°
- VMM parameter tuning: Peaking time: 25ns, 50 ns

Many studies were conducted to understand the sTGC detector response under such realistic background radiation conditions. One of the goals for the sTGC data measurements was to study the pad efficiency using a 4-scintillator coincidence: two scintillator coincidences from 2 GIF scintillators (dimensions: 40 cm · 40 cm) and two from 2 sTGC scintillators (dimensions: 4 cm · 15 cm with small overlap of 2 cm · 5 cm). A small rate detector is placed next to the ^{137}Cesium source to monitor the background rate per source attenuation filter.

The following GIF^{++} setup was used: the H4 beam line, the radiation source, the small rate detector, the sTGC quadruplet (placed in a downstream position from the radiation source) and the 4-scintillator coincidence (Figure 6.4).

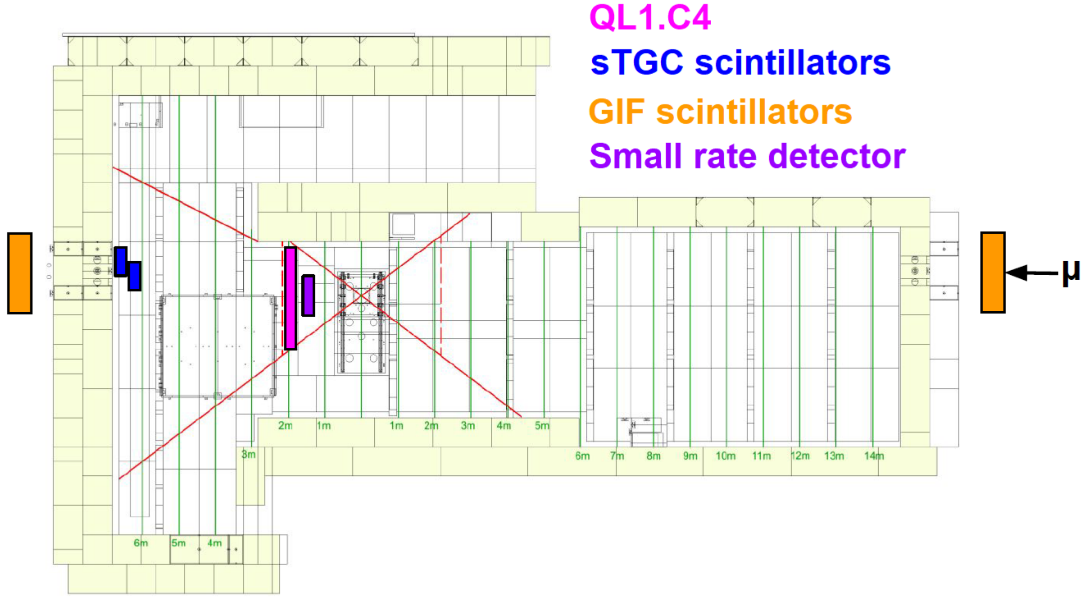

Figure 6.4: Schematics of GIF^{++} bunker, including the 4-scintillator coincidence. [39]

Due to the beam size, approximately one pad per sTGC layer is inside the beam region (pad pitch: 8 cm). These four physical pads are staggered, creating a common region that is called a logical pad tower (Figure 6.5). The 4-scintillator coincidence region is smaller than the logical pad which requires the pad efficiency calculation to derive from 3 out 4 hits on that logical pad tower.

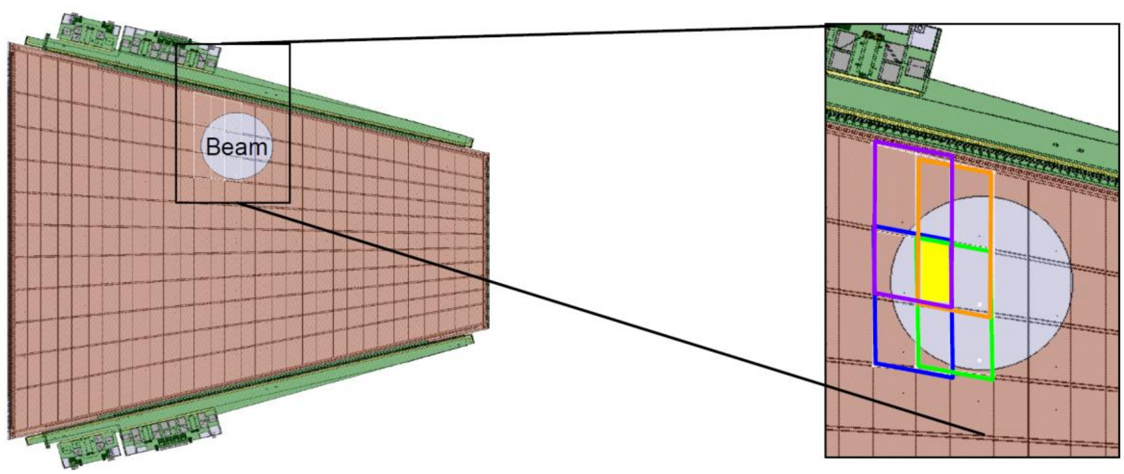

Figure 6.5: sTGC physical pads forming one logical pad area inside the beam region at GIF^{++} setup. [39]

6.3 Analysis with NSWRead

For the pad efficiency studies, different source attenuation filters and pulse peaking times were used to calculate the efficiency of each sTGC pad in one logical pad tower. The data analysis was performed using NSWRead, the main Data Quality Monitoring (DQM) framework for the ATLAS experiment. NSWRead reads ATLAS raw data either from a file or from a memory buffer (for online monitoring) into C++ data structures. It includes various applications that produce histograms for Data Acquisition Quality (DAQ) monitoring and performance studying of the NSW detectors.

The objective of the analysis is to understand the detector behavior without the photon contribution from the gamma irradiation source. In addition to the regular muon beam provided to the irradiation bunker, muons were also generated by a high intensity pion beam. Since both muons and pions are minimum ionizing particles with similar energy loss rate (Appendix A), we proceed the data analysis considering both types of beams and focusing on data generated only from muon/pion interactions. The four physical pads inside the 4-scintillator coincidence are:

Layer	No. Physical Pad
4	53
5	54
6	59
7	60

Table 6.1: Pad numbering of the four physical pads per layer in the 4-scintillator coincidence.

Additionally, a background rate scan was performed per source attenuation filter using the small rate detector (Figure 6.6).

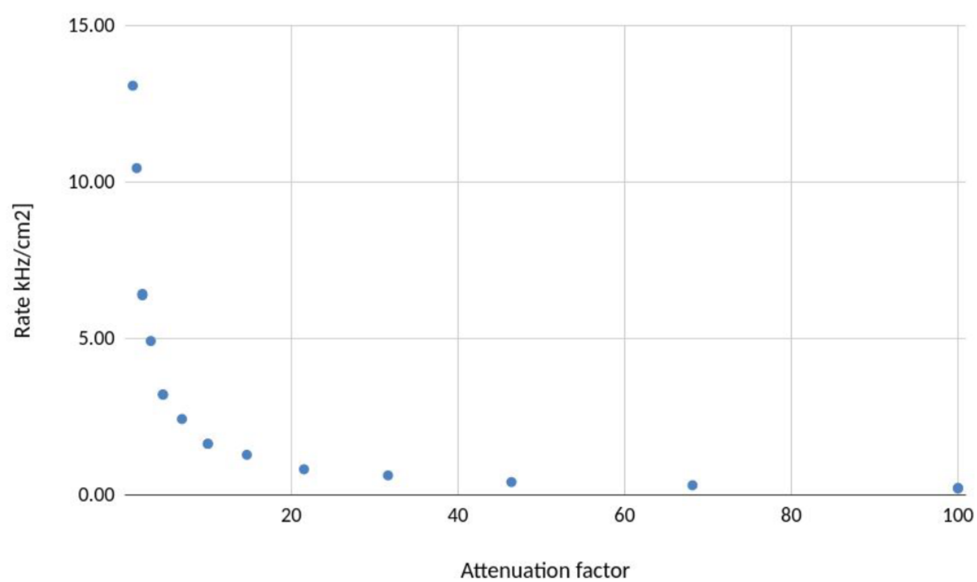

Figure 6.6: Rate scan per source attenuation factor at GIF^{++} setup. [39]

6.3.1 Calculating photon rate per pad surface

During data taking, an 8 BC (200 ns) data readout window was used to record incoming particles: muons/pions from the test beam and emitted photons from the gamma irradiation source. A theoretical calculation is performed to measure the probability of detecting a photon inside that data readout window, which follows a Poisson distribution:

$$P(x) = \frac{\lambda^x e^{-\lambda}}{x!}$$

where x =1, λ the mean number of occurrences over the given interval of 8 BC and e the Euler's constant. In Table 6.2 the probability results per pad are summarized. The photon rate per pad was utilized and calculated using the following relation:

$$f_{pad} = A_{pad} * 13\ kHz/cm^2$$

where A_{pad} the area of each pad, multiplied by the gamma irradiation source rate.

Layer	**No. Physical Pad**	$\boldsymbol{A_{pad}\ (cm^2)}$	$\boldsymbol{f_{pad}}$ **(MHz)**	$\boldsymbol{\lambda = \frac{200}{T_{pad}}}$	$\boldsymbol{P_{pad}}$ **(%)**
4	53	126.99	1.651	0.330	23.73
5	54	142.24	1.849	0.369	25.54
6	59	144.82	1.883	0.376	25.83
7	60	125.89	1.636	0.327	23.59

Table 6.2: Per pad probability of detecting a photon inside the 8 BC data readout window that was used.

The source rate is significantly high, which results in a non-negligible probability to record photon pad hits. Subsequently, the probability to detect a photon in x out 4 pads will follow a Binomial distribution:

$$P(x; p, n) = \binom{n}{x} p^x q^{n-x} = \binom{n}{x} p^x (1-p)^{n-x}$$

where n = 4 the number of layers, x = 0,1,2,3,4 the number of pad coincidences and p = probability of a photon pad coincidence in an event. Using P_{pad} probabilities from Table 6.2 as p, the binomial probabilities for a 3/4 and 4/4 pad coincidences are:

- $P_{\frac{3}{4}} = \big(0.2373 \cdot 0.2554 \cdot 0.2583 \cdot (1 - 0.2359)\big) + (0.2373 \cdot 0.2554 \cdot (1 - 0.2583) \cdot 0.2359) + (0.2373 \cdot (1 - 0.2554) \cdot 0.2583 \cdot 0.2359) + ((1 - 0.2373) \cdot 0.2554 \cdot 0.2583 \cdot 0.2359) = 0.045$ $\rightarrow\ P_{\frac{3}{4}} = 4.5\ \%$

- $P_{\frac{4}{4}} = 0.2373 \cdot 0.2554 \cdot 0.2583 \cdot 0.2359 = 0.0037\ \rightarrow P_{\frac{4}{4}} = 0.37\ \%$

We observe that, although the source rate is considerably high, the probability of a photon actually producing a pad coincidence in our pad pattern is small.

6.3.2 Calculating fake triggers from photons

A pad coincidence in our pad pattern can be produced from photon triggers when the gamma irradiation source is activated. Consequently, it is required to analytically calculate the percentage of such fake triggers using data from runs with various attenuation filters. We apply this calculation on a quad region outside the beam area (Figure 6.7), where we do not expect muon/pion pad hits, to measure only the γ contribution. A pad pattern is formed in the following pads:

Layer	No. Physical Pad
4	38
5	39
6	38
7	39

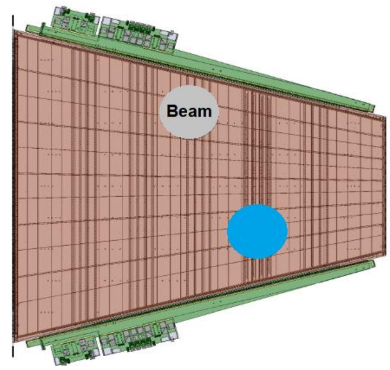

Figure 6.7: Pad numbering (left) for a pattern outside the test beam area of the 4-scintillator coincidence (depicted with a blue circle on the right).

Table 6.3 summarizes the percentage of photon pad coincidences in 3/4 and 4/4 layers for the pad pattern that was chosen. The percentage was calculated by measuring N the total number of events that produced these coincidences.

Peaking Time (ns)	Attenuation Filter	N_{events}	$N_{3/4}$ coincidences	$N_{4/4}$ coincidences	$\frac{N_{3/4} + N_{4/4}}{N_{events}}$ (%)
50	1	12909	105	3	0.84
25	1	491981	1135	38	0.24
50	1.5	14062	98	2	0.71
25	1.5	5111	23	1	0.47
50	2.2	44224	100	4	0.24
25	2.2	13130	26	0	0.20

Table 6.3: Photon pad coincidences for a pad pattern outside the beam area, using different attenuation filters and pulse peaking time: 50 ns and 25ns.

The percentage of fake triggers for one pad pattern is very small, with respect to the number of events in each run, but is increasing significantly for ~330 pad patterns that exist per quad. This has proven to be an important issue when the gamma irradiation source is activated. The differentiation between fake triggers and muon/pion triggers is difficult due to the large photon background.

6.3.3 Calculating pad efficiencies

The pad efficiency analysis was performed by applying the following selection criteria:

- **Strip clustering**
  Strip clusters are formed near the interaction point every time a particle traverses the sTGC detectors. When the irradiation source is not activated, additional strip clusters can still be produced from background noise that surrounds the detector. For this reason, correlating the data readout information from sTGC pads and sTGC strips per event is important in the pad efficiency studies.

  One strip cluster per layer is required, formed inside the 4-scintillator coincidence region (Figure 6.8). This condition should be met for all four layers, before calculating the pad efficiencies, in order to ensure that the coincidence was produced by a traversing muon/pion inside the region of interest.

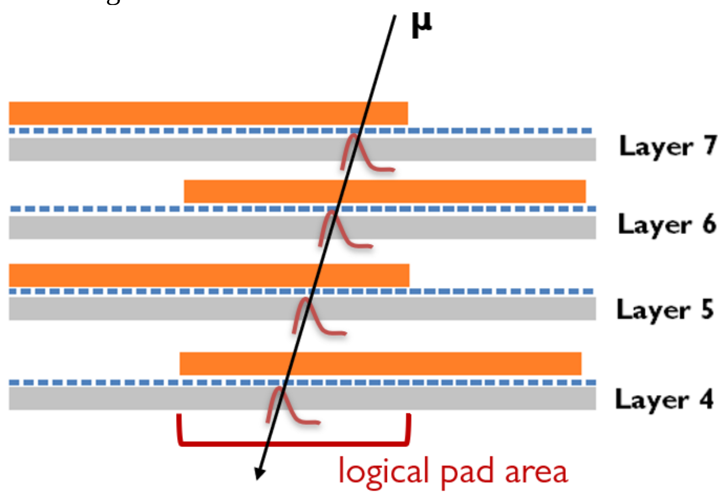

  Figure 6.8: Accepted event, producing strip clusters in every layer inside the region of interest. sTGC pads are depicted with orange color and sTGC strips with blue color.

- **PDO filter**
  We utilize the analog pulse information from each VMM channel to filter the Peak Detector Output (PDO) of each pad hit. PDO derives from the charge amplitude measurement of each pulse signal. We eliminate pad hits with charge overflow (≥ 1022 ADC counts), which derive from background noise, electronic issues, data pileup, emitted delta rays etc.

- **Trigger time calibration**
  For each VMM channel, a timing calibration was additionally performed between the scintillator trigger pulse and the recorded trigger pulse at the VMM. Two parameters are used: the relative BCID, the relative timing distance in BC between a trigger's BCID and the first BCID in that data readout window, and the Time Detector Output (TDO) which is collected from the pulse timing measurement using a Time-to-Amplitude Converter (TAC) [40].

The following relation is applied on each pad hit:

$$Trigger\_time = 25\,ns\ \times (\,relBCID\ -\ \frac{\mathrm{TDO}\ - \mathrm{TDO_{min}}}{\mathrm{TDO_{max}} - \mathrm{TDO_{min}}})$$

where the TDO min/max values from each VMM channel are used. In order to convey the correct timing information per layer in the analysis, the main requirement is to have a trigger time difference between layers at ≤ 30 ns.

The pad efficiency and the standard error of each pad efficiency calculation, was measured using the following relations:

$$eff = \frac{N_{\frac{4}{4}}}{N_{\frac{3}{4}}+N_{\frac{4}{4}}} \quad , \quad \sigma_{eff} = \sqrt{\frac{eff\cdot(1-eff)}{N_{\frac{3}{4}}+N_{\frac{4}{4}}}}$$

where N the number of events with 3/4 and 4/4 pad coincidence. Table 6.4 summarizes the efficiency results at pulse peaking time: 25 ns and 50 ns for each pad inside the 4-scintillator coincidence respectively.

Run number	**Pulse peaking time (ns)**	$\boldsymbol{eff} \pm \boldsymbol{\sigma_{eff}}$ **(%)**			
		Layer 4	**Layer 5**	**Layer 6**	**Layer 7**
1635414686	50	95.48 ± 0.14	96.02 ± 0.14	95.40 ± 0.15	90.41 ± 0.20
1635411486	50	94.94 ± 0.15	96.04 ± 0.13	95.13 ± 0.15	90.37 ± 0.20
1635725393	25	94.84 ± 0.23	96.46 ± 0.19	94.98 ± 0.22	88.45 ± 0.32
1635611713	25	93.59 ± 0.20	95.17 ± 0.18	93.12 ± 0.21	82.72 ± 0.29

Table 6.4: Pad efficiency results per layer for pulse peaking time: 25 ns and 50ns using source OFF runs. Trigger time calibration between layers applied at ≤ 30 ns.

According to the analysis results of Table 6.4, a pad efficiency greater than 82% is observed, both for 50 ns and 25 ns pulse peaking time. However, the sTGC pad on Layer 7 produces consistently lower efficiency results, with respect to other pads in the 4-scintillator coincidence. This behavior is still under investigation and could be related to VMM parameter configurations or geometrical correlation between pads.

6.3.4 Calculating MPV

When a charged particle traverses a gaseous detector, as are the sTGC detectors, one of the main electromagnetic interactions that occur with the gas molecules is ionization. Experimentally, the energy deposition distribution from such interactions has large fluctuations and follows a Landau distribution, where the most probable energy loss is lower than the mean energy loss (Appendix A). The Landau fluctuation is caused primarily by the rare but measurable occurrence of knock-on electrons (delta rays), which gain enough energy from the interaction to become ionizing particles themselves. The direction of the knock-on electron is typically perpendicular to the direction of the incoming particle, which causes irregular charge clouds and degrades spatial resolution [41].

We observe the PDO distribution to be in agreement with the expected behavior. Thus, the PDO - Most Probable Value (MPV) can be calculated by applying a Landau distribution fit (Figure 6.9).

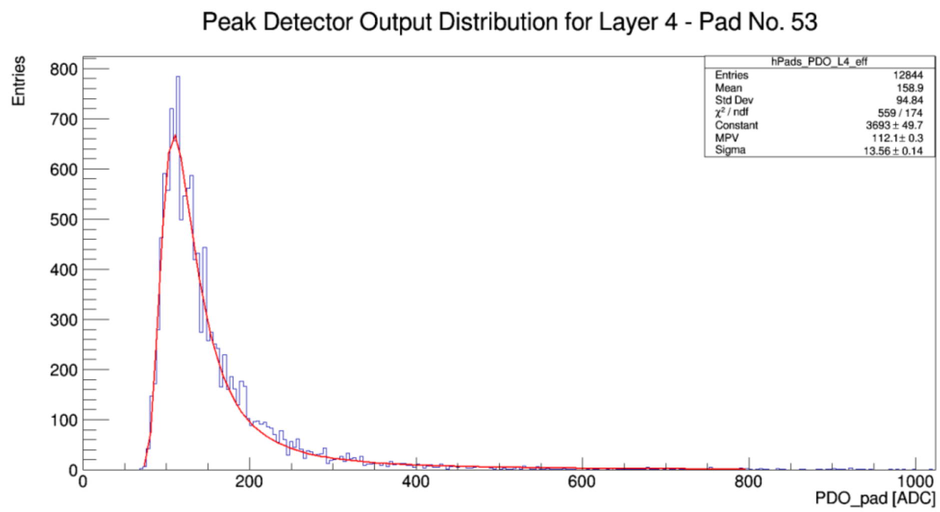

Figure 6.9: PDO distribution of a pad inside the 4-scintillator coincidence. A Landau fit is applied to calculate the MPV (depicted with a red line).

Table 6.5 summarizes the PDO-MPV at pulse peaking time: 25 ns and 50 ns for each physical pad inside the 4-scintillator coincidence respectively.

Run number	**Pulse peaking time (ns)**	**MPV ± σ_{MPV}**			
		Layer 4	**Layer 5**	**Layer 6**	**Layer 7**
1635414686	50	119.2 ± 0.2	134.5 ± 0.3	137.9 ± 0.3	114.8 ± 0.2
1635411486	50	119 ± 0.2	134.4 ± 0.3	137.4 ± 0.3	114.7 ± 0.2
1635725393	25	111.6 ± 0.3	123.7 ± 0.4	131 ± 0.4	112.8 ± 0.3
1635611713	25	111.4 ± 0.3	122.9 ± 0.3	129.4 ± 0.3	110.4 ± 0.2

Table 6.5: PDO MPV results per layer for pulse peaking time: 25 ns and 50ns using source OFF runs. Trigger time calibration between layers applied at ≤ 30 ns.

It is evident from the PDO-MPV results that a pulse peaking time of 50 ns duration allows the VMM to collect sufficient information from the pulse signal.

6.3.5 Calculating Pad Trigger efficiency

In the sTGC trigger path, the pulse information from pad FEBs is conveyed to the Pad Trigger at the sTGC rim crate. During the sTGC data taking at GIF^{++}, the trigger path did not include a PT and all data was directly readout as recorded from the pad and strip FEBs. Our objective is to study the theoretical response of the PT under these conditions and measure its efficiency in processing data that derive from a high-rate background.

The efficiency of the PT depends directly on the pad efficiency of each pad inside the 4-scintillator coincidence. The probability to detect a pad hit in x out 4 pads follows the Binomial distribution:

$$P(x;p,n) = \binom{n}{x} p^x q^{n-x} = \binom{n}{x} p^x (1-p)^{n-x}$$

where n = 4 the number of layers, x = 0,1,2,3,4 the number of pad coincidences and p = probability to have a pad hit in a layer per event. Using the pad individual efficiencies from Table 6.4 as p, the probability relations for a 3/4 and 4/4 pad coincidences are:

- $P_{\frac{3}{4}} = \left(\mathrm{eff_{L4}} \cdot \mathrm{eff_{L5}} \cdot \mathrm{eff_{L6}} \cdot (1 - \mathrm{eff_{L7}})\right) + (\mathrm{eff_{L4}} \cdot \mathrm{eff_{L5}} \cdot (1 - \mathrm{eff_{L6}}) \cdot \mathrm{eff_{L7}}) + (\mathrm{eff_{L4}} \cdot (1 - \mathrm{eff_{L5}}) \cdot \mathrm{eff_{L6}} \cdot \mathrm{eff_{L7}}) + ((1 - \mathrm{eff_{L4}}) \cdot \mathrm{eff_{L5}} \cdot \mathrm{eff_{L6}} \cdot \mathrm{eff_{L7}})$
- $P_{\frac{4}{4}} = \mathrm{eff_{L4}} \cdot \mathrm{eff_{L5}} \cdot \mathrm{eff_{L6}} \cdot \mathrm{eff_{L7}}$

Upon event selection, the PT makes trigger decision based on coincident hits in 3-out-of-4 layers in each sTGC quadruplet. For this reason, the total Pad Trigger efficiency is given by:

$$PT_{eff} = P_{\frac{3}{4}} + P_{\frac{4}{4}}$$

Although it is an estimation, in Table 6.6 we can observe promising efficiency results, greater than 96%, for the operation of the PT.

Run number	**Pulse peaking time (ns)**	$\boldsymbol{PT_{eff}}$ (%)
1635414686	50	98.30
1635411486	50	98.16
1635725393	25	97.95
1635611713	25	96.19

Table 6.6: Pad Trigger efficiency results per layer for pulse peaking time: 25 ns and 50ns using source OFF runs. Trigger time calibration between layers applied at ≤ 30 ns.

Chapter 7

Conclusions

In this thesis, the response of the trigger system for the New Small Wheel muon detector electronics was studied in two parts. The thesis's objective was to validate the operation of the trigger electronics and contribute to the verification of its operation.

The first part summarizes the creation of a python tool, used to configure the ATLAS Local Trigger Interface with simulated triggers. The tool's features and parameters were described. A series of data readout tests were performed at Vertical Slice Lab, where ALTI was programmed with various pulse pattern files that were produced by the program. Data analysis focused on signal transmission by/to the individual NSW sTGC trigger electronics. The response of the trigger system produced promising results under clocked and random trigger conditions.

The second part includes the data analysis with NSW sTGC detectors at GIF^{++}. The detectors were exposed to a muon/pion beam combined with irradiations from a ^{137}Cs source. Emphasis was laid on sTGC pad efficiency studies under such realistic trigger and background radiation conditions. The chosen methodology for the individual sections of the analysis was presented, along with the analysis results. The pad sTGC detector response was very good, with efficiency results greater than 82%. Additional theoretical calculations were performed to gain a better understanding of the detector response.

Appendix A

Interaction of charged particles with matter

In particle physics experiments, various techniques are employed to detect and identify produced particles from high-energy collisions. Knowing the interaction of the particle with the detector material in detail allows us to deduce precise and quantitative information about the particle properties.

Charged particles interact with matter through well-known electromagnetic processes such as: excitation, ionization, production of Cherenkov radiation and Bremsstrahlung radiation. In these processes, particles lose a fraction of their energy and velocity as they travel through matter and continuously interact with the electrons and atom nuclei. The mean rate of energy loss per unit length (stopping power) of a charged particle is described by the Bethe-Bloch equation:

$$-\langle\frac{dE}{dx}\rangle = K\rho\frac{Z}{A}\frac{z^2}{\beta^2}[\ln\frac{2m_e c^2\gamma^2\beta^2 T_{max}}{I^2} - 2\beta^2 - \delta - 2\frac{C}{Z}]$$

where:

- $K = 2\pi N_a r_e^2 m_e c^2 = 0.1535\, MeV \cdot cm^2/g$ with N_a the Avogadro number, r_e the classical electron radius, m_e the electron rest mass and c the speed of light
- ρ the density of the absorbing material
- z the charge of the incident particle
- A the atomic mass number of the medium
- Z the atomic number of the medium
- $\beta = \frac{v}{c}$ the velocity of the incident particle
- $\gamma = \frac{1}{\sqrt{1-\beta^2}}$ the Lorentz factor
- I the mean excitation energy of the medium
- T_{max} the maximum kinetic energy which can be imparted to a free electron in a single collision
- δ the density correction: the electric field of the particle tends to polarize atoms along its path, shielding electrons (far from the particle path) from full electric field intensity
- $\frac{C}{Z}$ the shell correction: arises if the velocity of incident particle is comparable to the orbital velocity of bound electrons ($v_{incident} \sim v_{orbit}$)

Upon further analysis of the Bethe-Bloch formula, one can determine that there is no explicit dependence on the incident particle's mass even though it can be used for particle identification (Figure A.2), it has a weak dependence on the material, entering via the term $\frac{Z}{A}$ which is roughly constant, and it depends quadratically on the particle's charge z and velocity β.

The stopping power for positive muons in copper can be seen in Figure A.1. The Bethe-Block equation is not yet valid for slow particles at βγ < 0.01 (shell correction). At low energies where 0.01 < βγ < 1, it is dominated by the $\frac{1}{\beta^2}$ factor. The mean energy loss decreases with increasing velocity until $v = 0.96 \cdot c$ where the minimum value is reached at βγ ≃ 3-4. Particles in this energy range (~1 – 2.0 $MeV\ cm^2/g$) are also known as minimum ionizing particles (MIP). For βγ > 3, the formula depends logarithmically on βγ resulting in a slow relativistic rise of the mean energy loss rate. Radiative effects such as Bremsstrahlung are also evident at βγ > 1000, where $\frac{dE}{dx}$ is not a function of βγ (δ correction).

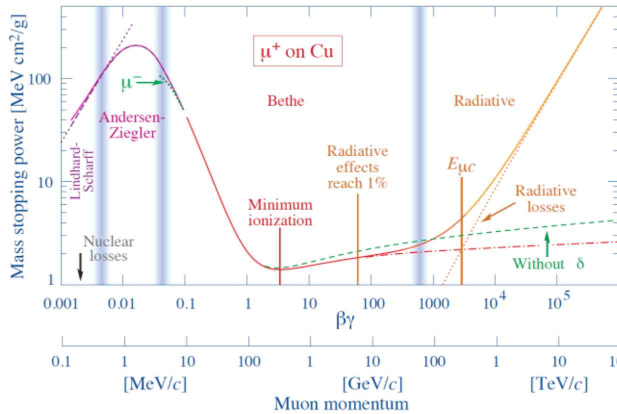

Figure A.1: Stopping power for positive muons in copper as a function of βγ and the muon momentum. The Bethe-Bloch formula is an excellent description in the range 0.1 < βγ < 100. The μ^- dotted lines illustrate the “Barkas effect,” the dependence of stopping power on projectile charge at very low energies. [42]

Measuring both the particle momentum and the energy loss rate allows charged particles to be identified (Figure A.2).

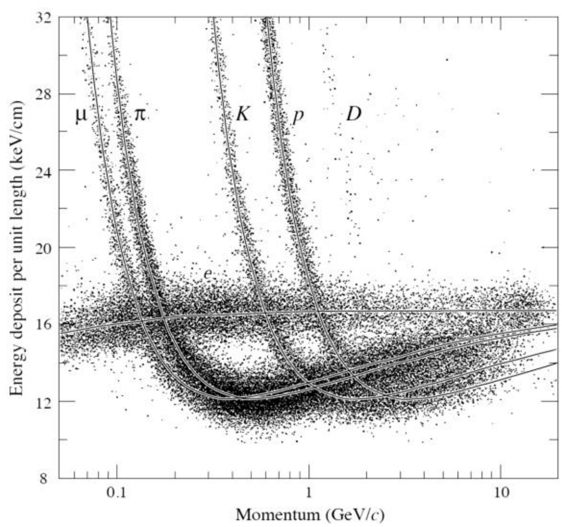

Figure A.2: Measured ionization energy loss of electrons, muons, pions, kaons, protons and deuterons as a function of momentum. The energy loss rate of electrons does not follow the Bethe-Bloch formula (dominant process is Bremsstrahlung). [43]

It should be noted that the Bethe-Bloch equation describes only the average energy loss. In general, energy losses of incident charged particles are a statistical phenomenon: collisions are independent events and their number varies from particle to particle. In each interaction different amounts of kinetic energy can be transferred to atomic electrons. For particles passing through a thin layer of absorber or a low-density material, the most probable energy loss is better described by a Landau distribution (or Landau-Vavilov):

$$\Delta_p = \xi [\ln \frac{2m_e c^2 \gamma^2 \beta^2}{I} + ln\frac{\xi}{I} + j - \beta^2 - \delta]$$

where $\xi = \left(\frac{K}{2}\right) \rho \frac{Z}{A} \frac{z^2}{\beta^2} x$ MeV for a detector with a thickness x in $g\ cm^{-2}$ and j = 0.2.

As seen in Figure A.3, a highly asymmetric distribution of the deposited energy is observed. The mean of the experimental distribution has large fluctuations and the most probable value is far lower than the average predicted by the Bethe Bloch equation. The "Landau tail" is a result of the very broad energy spectrum of knock-on electrons (δ-rays) emitted by close encounters with the atomic electrons.

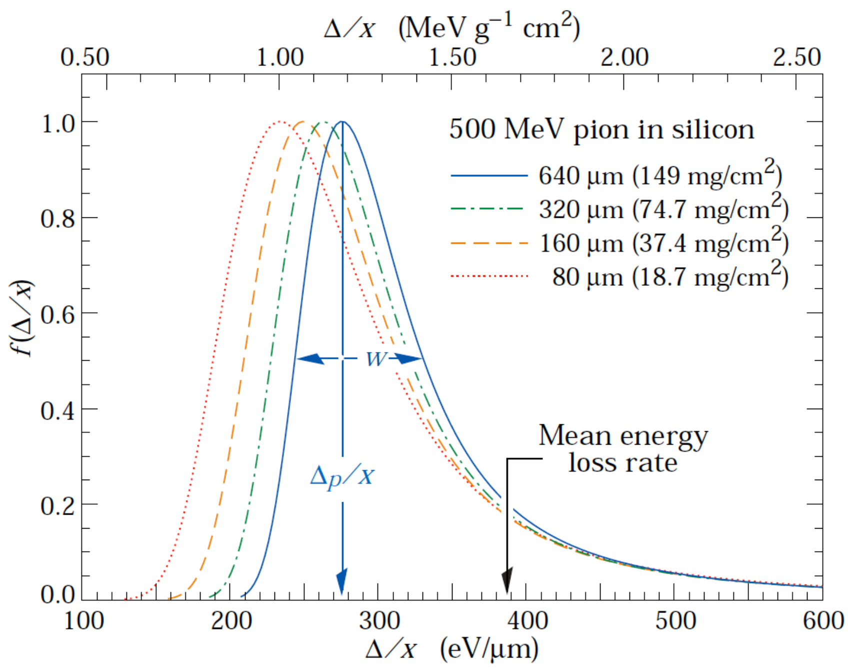

Figure A.3: Energy deposition distributions for different thickness of Si detectors. The fluctuation around the maximum of the Landau distribution becomes greater as the detector becomes thinner. [43]

The distribution becomes symmetrical again after a large number of interactions obtained from either a thick or dense material. The energy loss rate is then described by a Gaussian distribution, with a mean given by the Bethe-Bloch equation.

Bibliography

[1] "The CERN accelerator complex". *CERN Document Server*. Jan. 2022. Available: CERN-GRAPHICS-2022-001-1

[2] J. Jowett. "Outlook for Nuclear Collisions in the LHC after Run 2". *European Physical Society Conference on High Energy Physics, Ghent, Belgium.* July 2019. Available: https://indico.cern.ch/event/577856/contributions/3420374/

[3] B.G. Taylor. "Timing Distribution at the LHC". *8th Workshop on Electronics for LHC Experiments, Colmar, France*. Sep. 2002. DOI: 10.5170/CERN-2002-003.63

[4] W. Herr, B. Muratori. "Concept of luminosity". *CERN Accelerator School: Intermediate Course on Accelerator Physics, Zeuthen, Germany".* Sep. 2003. pp. 361–378. DOI: 10.5170/CERN-2006-002.361

[5] "Computer generated image of the whole ATLAS detector". *CERN Document Server*. Mar. 2008. Available: CERN-GE-0803012-01

[6] "How ATLAS detects particles: diagram of particle paths in the detector". *CERN Document Server*. Jan. 2013. Available: CERN-EX-1301009-01.

[7] T. Lenzi. "Development and Study of Different Muon Track Reconstruction Algorithms for the Level-1 Trigger for the CMS Muon Upgrade with GEM Detectors". *arXiv:1306.0858 ; CERN-THESIS-2013-042*. Available: http://cds.cern.ch/record/1551944

[8] "Computer generated image of the ATLAS inner detector". *CERN Document Server*. Mar. 2008. Available: CERN-GE-0803014-01

[9] "Computer Generated image of the ATLAS calorimeter". *CERN Document Server*. Mar. 2008. Available: CERN-GE-0803015-01

[10] "Computer generated image of the ATLAS Muons subsystem". *CERN Document Server*. Mar. 2008. Available: CERN-GE-0803017-01

[11] ATLAS Collaboration. "ATLAS New Small Wheel Technical Design Report". *CERN-LHCC-2013-006 ; ATLAS-TDR-020.* June 2013. Available: https://cds.cern.ch/record/1552862

[12] "ATLAS Detector Magnet System". *CERN Document Server*. May 2021. Available: ATLAS-PHOTO-2021-029

[13] J.J. Goodson. "Search for Supersymmetry in States with Large Missing Transverse Momentum and Three Leptons including a Z-Boson". *CERN-THESIS-2012-053*. Apr. 2012. Available: https://cds.cern.ch/record/1449722

[14] ATLAS Collaboration. "ATLAS: technical proposal for a general-purpose pp experiment at the Large Hadron Collider at CERN". *CERN-LHCC-94-43 ; LHCC-P-2*. 1994. DOI: 10.17181/CERN.NR4P.BG9K

[15] W.P. Vazquez. "The ATLAS Data Acquisition System: from Run 1 to Run 2". *37th International Conference on High Energy Physics, Valencia, Spain.* July 2014. DOI: 10.1016/j.nuclphysbps.2015.09.146

[16] ATLAS Collaboration. "ATLAS level-1 trigger: Technical Design Report". *CERN-LHCC-98-014 ; ATLAS-TDR-12*. June 1998. Available: https://cds.cern.ch/record/381429

[17] ATLAS Collaboration. "ATLAS high-level trigger, data-acquisition and controls: Technical Design Report". *CERN-LHCC-2003-022 ; ATLAS-TDR-16*. July 2003. Available: https://cds.cern.ch/record/616089

[18] "LHC/ HL-LHC Plan". Feb. 2022. Available: https://hilumilhc.web.cern.ch/content/hl-lhc-project

[19] ATLAS Collaboration. "ATLAS Liquid Argon Calorimeter Phase-I Upgrade : Technical Design Report". *CERN-LHCC-2013-017 ; ATLAS-TDR-022*. Sep. 2013. Available: https://cds.cern.ch/record/1602230

[20] ATLAS Collaboration. "Technical Design Report for the Phase-I Upgrade of the ATLAS TDAQ System". *CERN-LHCC-2013-018 ; ATLAS-TDR-023*. Sep. 2013. Available: https://cds.cern.ch/record/1602235

[21] S. Veneziano. "Functional diagram of the ATLAS Trigger and Data Acquisition system in Run 3". *ATLAS Twiki*. Available: https://twiki.cern.ch/twiki/bin/view/AtlasPublic/ApprovedPlotsDAQ

[22] A. Canesse. "Small-Strip Thin Gap Chambers for the Muon Spectrometer Upgrade of the ATLAS Experiment". *PoS(LHCP2020)245*. May 2020. DOI: https://doi.org/10.22323/1.382.0245

[23] P. Miao et al. "The development of the Front-End Boards for the small-strip Thin Gap Chambers detector system of the ATLAS Muon New Small Wheel upgrade". *JINST* **15** P11024. Nov. 2020. DOI: 10.1088/1748-0221/15/11/P11024

[24] K. Ntekas. "Performance studies of resistive Micromegas chambers for the upgrade of the ATLAS Muon Spectrometer". *EPJ Web Conf. 174 (2018) 01014.* Feb. 2018. DOI: 10.1051/epjconf/201817401014

[25] Y. Horri. "ATLAS/CMS Upgrades". *14th Conference on Flavor Physics and CP Violation, Pasadena, California, USA.* June 2016. Available: https://cds.cern.ch/record/2160231

[26] P. Scholer. "Test Beam Results and Performance Studies of ATLAS Micromegas Production Modules". *J. Phys.: Conf. Ser.* **1498** 012053. 2020. DOI: https://doi.org/10.1088/1742-6596/1498/1/012053

[27] L. Levinson. “NSW electronics overview”. Oct. 2021. Available: https://espace.cern.ch/ATLAS-NSW-ELX

[28] X. Wang. “Frontend and backend electronics for the New Small Wheel Upgrade of the ATLAS muon spectrometer”. *TWEPP 2018 Topical Workshop on Electronics for Particle Physics*. Sep. 2018. Available: https://indico.cern.ch/event/697988/contributions/3055968/

[29] S. Sánchez. “Implementation of the ROD Crate DAQ Software for the ATLAS Tile Calorimeter and a Search for a MSSM Higgs Boson decaying into Tau pairs”. *CERN-THESIS-2010-162*. Nov. 2010. Available: https://cds.cern.ch/record/1309926

[30] E. Simioni. “The Topological Processor for the future ATLAS Level-1 Trigger: from design to commissioning”. *19th IEEE-NPSS Real Time Conference, Nara, Japan*. May 2014. Available: http://cds.cern.ch/record/1741145

[31] S. Ask et al. “The ATLAS Central Level-1 Trigger Logic and TTC”, *JINST* **3** P08002. Aug. 2008. DOI: 10.1088/1748-0221/3/08/P08002

[32] P. Kuzmanović. “Development and Testing of the ALTI Module for Timing and Synchronization in the ATLAS experiment at CERN”. *CERN-THESIS-2018-335*. Sep. 2018. Available: https://cds.cern.ch/record/2655027

[33] EP-Electronic Systems for Experiments Group (CERN). “The ALTI module”. Available: https://ep-ese.web.cern.ch/project/atlas-alti

[34] C. Clement. “ATLAS Trigger "sur le terrain"”. *Physique ATLAS France, Evian*. Oct. 2009. Available https://indico.cern.ch/event/68358/contributions/1234806/

[35] The ATLAS FELIX Project. Available: https://atlas-project-felix.web.cern.ch/atlas-project-felix/

[36] R. Vari. “Pad trigger integration status and readout”. *ATLAS Muon & NSW week [Online]*. Feb. 2020. Available: https://indico.cern.ch/event/882570/#4-pad-trigger-integration-stat

[37] D. Pfeiffer et al. “The radiation field in the Gamma Irradiation Facility GIF++ at CERN”. *Nuclear Instruments and Methods in Physics Research, A **866***. pp. 91-103. Sep. 2017. DOI: https://doi.org/10.1016/j.nima.2017.05.045

[38] R. Margraf, N. Charitonidis. “Muon Beam Studies in the H4 beam line and the Gamma Irradiation Facility (GIF^{++})”. *CERN-ACC-NOTE-2018-0029*. Mar. 2018. Available: http://cds.cern.ch/record/2310593

[39] K. Solovieva. “sTGC beam test in GIF^{++}: status and plans”. *ATLAS New Small Wheel General Meeting [Online]*. Oct. 2021. Available: https://indico.cern.ch/event/1090484/#8-stgc-beam-test-in-gif-status

[40] G. De Geronimo, V. Polychronakos and G. Iakovidis. "ATLAS NSW Electronics Specifications: Component VMM3a". Oct. 2017. Available: https://twiki.cern.ch/twiki/pub/Atlas/NSWelectronics/vmm3a.pdf

[41] S. Meroli. “The Landau distribution for ionizing particles”. Available: https://meroli.web.cern.ch/lecture_landau_ionizing_particle.html

[42] P.A. Zyla et al. (Particle Data Group). *Prog. Theor. Exp. Phys.* ***2020****, 083C01 (2020) and 2021 update*. Available: http://pdg.lbl.gov/

[43] A. Tapper. “Introduction to Detectors”. *Lecture: Instrumentation & Detectors Overview*. Available: http://www.hep.ph.ic.ac.uk/~tapper/lecture/Detectors-Full.pdf

List of Abbreviations and Acronyms

ADDC	ART Data Driver Card
ALICE	A Large Ion Collider Experiment
ALTI	ATLAS Local Trigger Interface
ASIC	Application Specific Integrated Circuits
ATLAS	A Toroidal LHC ApparatuS
BC	Bunch Crossing
BCID	Bunch Crossing Identification
BCR	Bunch Counter Reset
BPM	Bi-Phase Mark
CERN	Conseil Européen pour la Recherche Nucléaire
CMS	Compact Muon Solenoid
CS	Central Solenoid magnet
CSC	Cathode Strip Chambers
CTP	Central Trigger Processor
DAQ	Data Acquisition Quality
DCN	Data Collection Network
DCS	Detector Control System
DQM	Data Quality Monitoring
ECR	Event Counter Reset
FEB	Front-End Board
FELIX	Front-End Link Interface Exchange
FEX	Feature EXtractor board
FPGA	Field Programmable Gate Array
GBT	GigaBit Transceiver
GIF	Gamma Irradiation Facility
HL-LHC	High-Luminosity Large Hadron Collider
HLT	High Level Trigger system
IP	Interaction Point
L1A	Level-1 trigger accept signal
L1Calo	Level-1 LAr calorimeter trigger system
L1DDC	Level-1 Data Driver Card
L1Muon	Level-1 Muon trigger system
L1Topo	Level-1 Topological trigger system
LAr	Liquid Argon calorimeter
LEP	Large Electron–Positron Collider
LHC	Large Hadron Collider
LHCb	Large Hadron Collider beauty
Linac4	Linear accelerator 4
LS2	Long Shutdown II
LTP	Local Trigger Processor
LTPI	Local Trigger Processor Interface
LUT	Look-up Table
LVDS	Low-Voltage Differential Signaling
LVL1	Level-1 trigger system
LVL2	Level-2 trigger system

MDT	Monitored Drift Tubes (MDT)
MM	Micro-Mesh Gaseous Structure detector
MPV	Most Probable Value
MuCTPI	Muon to Central Trigger Processor Interface
NSW	New Small Wheel
OPC UA	Open Platform Communications Unified Architecture
PCB	Printed Circuit Board
PDO	Peak Detector Output
PS	Proton Synchrotron
PSB	Proton Synchrotron Booster
PT	Pad Trigger
ROC	Readout Controller
ROD	Read-Out Drivers
RoI	Regions of Interest
ROS	Read-Out System
RPC	Resistive Plate Chambers
SBC	Single-Board Computer
SCA	Slow Control Adapter
SCT	Semiconductor Tracker
SFO	Sub-Farm Output
SFP	Small Form-factor Pluggable
SPS	Super Proton Synchrotron
sTGC	small-strip Thin Gap Chamber
TAC	Time-to-Amplitude Converter
TDAQ	Trigger and Data Acquisition
TDO	Time Detector Output
TDS	Trigger Data Serializer
TDM	Time Division Multiplexing
TGC	Thin Gap Chamber
TileCal	Tile Calorimeter
ToT	Time-over-Threshold
TRT	Transition Radiation Tracker
TTC	Timing, Trigger and Control system
TTCex	TTC Encoder/Transmitter
TTCvi	TTC VMEbus Interface (TTCvi)
VMEbus	Versa Module Europa bus

List of Figures

List of Tables

Page